ABraytCSPfuture

Air-Brayton Cycle Concentrated Solar Power future plants via redox oxides-based structured thermochemical heat exchangers / thermal boosters

Deliverable D3.2.
Optimal porous structures for combined TCS/thermal booster operation

Dissemination Level: SEN

WP3 Preparation of lab-scale redox oxides porous structured test specimens and application-specific testing

Date: 31.01.2025

https://www.abraytcspfuture.eu/

This project has received funding from the European Union's Horizon Europe research and innovation programme under grant agreement no 101084569.

Disclaimer

The work described in this document has been conducted within the ABraytCSPfuture project that is co-funded by the European Union. Views and opinions expressed herein are however those of the author(s) only and do not necessarily reflect those of the European Union or of the granting authority, European Climate, Infrastructure and Environment Executive Agency (CINEA). Neither the European Union nor the granting authority can be held responsible for them.

Grant Agreement Number: 101084569 Acronym: ABraytCSPfuture				
Full Title	**A**ir-**Brayt**on Cycle **C**oncentrated **S**olar **P**ower **future** plants via redox oxides-based structured thermochemical heat exchangers/thermal boosters			
Call Topic Identifier:	HORIZON-CL5-2021-D3-03			
Funding Scheme	HORIZON EUROPE, RIA – Research and Innovation Actions			
Project start date:	01.11.2022			
Project duration:	48 months			
Project URL	https://www.abraytcspfuture.eu/			
EU Project Officer	Clara Astudillo Llorente			
Project Coordinator	DLR – German Aerospace Center			
Deliverable	D3.2 – Optimal porous structures for combined TCS/thermal booster operation			
Date of Delivery	Contractual	31.01.2025	Actual	03.02.2025
Nature	Report			
Dissemination Level	Sensitive			
Lead Beneficiary	CERTH – Centre for Research and Technology Hellas			

Document History

Version	**Issue Date**	**Change History**	**Authors**	**Organisation**
1.0	26.01.2025	Document drafted	George Karagiannakis, Chrysa Pagkoura	CERTH
1.1	28.01.2025	Updated with final partner feedback	Christos Agrafiotis, David Vellas, Mathias Pein, Asmaa Eltayeb, Raisa Santana	DLR
1.2	31.01.2025	Final Review	Iñigo Muñoz	TEKN

About the Project

ABraytCSPfuture sets forth an innovative, carbon-neutral way for implementing the highly efficient air-Brayton gas turbine power generation cycles into future air-operated Concentrated Solar Power (CSP) plants. Air-Brayton cycles are used in traditional power plants where, however, involve fossil fuels combustion via pressurized air. *ABraytCSPfuture*'s carbon-neutral approach aims at achieving higher solar-to-electricity efficiencies, vital for competitiveness of CSP and non-reachable by either PVs or molten salts and thermal oils, increasing in parallel significantly the plants' storage capability. The project will develop and demonstrate a first-of-its-kind compact, dual-bed thermochemical reactor/heat exchanger unit that will transfer heat from a non-pressurised air stream to a pressurised one, while also operating as a thermal booster, raising the temperature of the pressurized stream to the level required for Brayton cycles. Furthermore, the volumetric solar energy storage density of air-operated CSP plants will be significantly increased by rendering their current sensible-only regenerative storage systems to hybrid sensible-thermochemical storage ones within the same storage volume. Both these functionalities will be materialized by thermochemical reactor/heat exchanger units comprised of non-moving, flow-through porous ceramic structures (honeycombs or foams) based on earth-abundant, cost-efficient, non-toxic oxide materials and exploiting reversible reduction/oxidation reactions of such oxides in direct contact with air, accompanied by significant endothermic/exothermic heat effects. The proposed technology is set forth by an interdisciplinary partnership spanning the entire CSP value chain, comprised of leading research centres, universities, innovative SMEs and large enterprises, including ancillary services providers and technology end-users.

Deutsches Zentrum fuer Luft- und Raumfahrt e.V., **DLR**	DE	DLR
Centre for Research & Technology Hellas, **CERTH**	EL	CERTH CENTRE FOR RESEARCH & TECHNOLOGY HELLAS
University of Twente, **UT**	NL	UNIVERSITY OF TWENTE.
Fundación CENER, **CENER**	ES	CENER ADItech
Fundación TEKNIKER, **TEKN**	ES	Tekniker
Fraunhofer Gesellschaft zur Foerderung der angewandten Forschung e.V., **FHG (IWKS)**	DE	Fraunhofer IWKS
OPRA Turbines, **OPRA**	NL	Destinus
KRAFTBLOCK GmbH, **KB**	DE	KRAFT BLOCK
LANDSON Emission Technologies A/S, **LET**	DK	landson
COBRA Instalaciones y Servicios S.A., **COBRA**	ES	cobra

Table of Contents

This deliverable is part of a project that has received funding from the European Union's Horizon Europe research and innovation programme under grant agreement no 101084569

Executive Summary

The present document contains results relating to the main properties of interest of structured small-scale redox bodies (honeycombs and foams) based on $CaMnO_3$ (CMO) perovskites. The information provided herein is based on experimental results produced in the frame of WP3 and spans from the assessment of multi-cyclic redox performance to the demonstration and quantification of heat effects during the oxidation of pre-reduced/charged structures, the assessment of the mechanical stability of these structures and the effect of multi-cyclic redox operation on their structural stability. Comparative physico-chemical analyses provide insights on the morphological, structural and compositional of the CMO-based bodies. A very important part of the results presented herein relates to a parametric study that provides valuable correlation of both redox- and energetic-related parameters to the operating parameters of the process targeted by ABCSPF project.

The results presented herein also provide solid **proof for the successful completion of project's milestone *M2: Structured objects made of optimized material compositions with maximum active material content selected for manufacture of the proof-of-concept unit*** to a large extent by M27. More specifically, two different redox geometries (one foam and one honeycomb, both from $Ca_{0.90}Sr_{0.10}MnO_3$ (CS10MO)) are identified as *able to demonstrate structural integrity & tolerable dimensional changes for at least 200 cycles* while yielding combined *TCS + sensible energy density ≥ 300 kWh/m³*. To be more precise, regarding the energy density target and tolerable dimensional changes these are already proven and confirmed here while with respect to the structural integrity there is solid evidence that this is maintained to a large extent, especially for the 59 cpsi CS10MO honeycomb. Final confirmation will be provided by additional measurements and analyses (i.e. crushing strength, scanning electron microscopy and Hg porosimetry) in the used/cycled structure already scheduled for the upcoming project period.

Changes with respect to the DoA

There are no notable changes referring to the DoA and thus the timely preparation of the present deliverable and implementation of the workplan of WP3, until submission of this deliverable, have not been affected.

1. Introduction

The present deliverable relates to small-scale optimal porous structures for combined TCS/thermal booster operation based on combined experimental results referring to their redox and energetic activity, thermomechanical stability and cyclability performance. The deliverable is directly associated with Tasks 3.2 and 3.3 and, considering the results presented herein, is the main means to assess the project's milestone *M2: Structured objects made of optimized material compositions with maximum active material content selected for manufacture of the proof-of-concept unit*.

The lab-scale structures prepared in Task 3.1 (please refer also to D3.1) were subjected to experimental evaluation to determine important operational parameters such as redox activity, energetic performance and cyclability in the frame of multi-cyclic campaigns (up to > 200 redox cycles) with the aid of a dedicated test rig built for this purpose. These parameters were determined over a wide range of operational conditions and for several different structures in order to define in-principle optimum conditions and decide on the general characteristics of the structured bodies to be considered for the scaled-up manufacturing and experimental evaluation in the frame of WP5 (in the short term) and WP6 (in the longer term). Of equal importance were also the correlations produced – and presented here in detail – to be used directly exploited as input for the modelling work in WP4 and facilitate the design of the targeted prototype system.

Moreover, the structures – together with reference ones to provide a direct comparison – were subjected to mechanical (i.e. crushing strength) measurements to assess their robustness. The thermomechanical performance was also assessed via comparative observations and analyses between pristine and used/multi-cycled specimens. The results, to be further enhanced by crushing strength measurements in used structures already scheduled for the next months, provide a first reliable picture on the ability of structured redox bodies to survive the challenging conditions of multi-cyclic thermal redox operation and can be used as guidelines for the scaling-up.

2. Redox thermochemical and energetic performance of lab-scale structured specimens

This section provides important aspects and quantitative results associated with the redox performance and calculated energy density of structured specimens manufactured in the frame of Task 3.1 (see also D3.1) from $CaMnO_3$ (CMO)-based compositions. The samples tested and their main characteristics are summarized in Table 1 below. Relevant photographs of the specimens can be found in deliverable D3.1. The evaluation is carried out via a dedicated in-house built test-rig at CERTH and the parameters of interest are assessed via both direct in-line measurements (i.e. oxygen released/consumed during reduction/oxidation) and calculations based on real-time temperature measurements during the redox performance, with special emphasis on the oxidation (discharging) step of the process. Details are provided in paragraph 2.1 below.

Structure composition	Structure geometry	Bulk density ($g \cdot cm^{-3}$)
$CaMnO_3$ (CMO)	Flow-through honeycomb with 111 channels per square inch (cpsi)	1.20
	Flow-through honeycomb with 59 channels per square inch (cpsi)	2.25
$Ca_{0.90}Sr_{0.10}MnO_3$ (CS10MO)	Flow-through honeycomb with 59 cpsi	2.10
	Foam with 60 pores per linear inch (ppi)	0.81

Table 1: Overview of structures subjected to multi-cyclic redox evaluation so far

2.1 The test-rig, operational protocols & main results for the structures evaluated so far

The targeted hybrid sensible/redox thermochemical energy storage scheme of ABrayCSPfuture (ABCSPF) is largely defined by the reaction enthalpy (ΔH_{rxn}) of its redox reaction. It is directly associated with the cyclic chemical reaction which provides the high energy storage density element of the overall heat storage concept. The redox equation for the specific case of CMO follows a non-stoichiometric scheme written as:

$$CaMnO_3 \leftrightarrow CaMnO_{3-\delta} + \tfrac{1}{2} \cdot \delta\ O_2,\ \Delta H_{rxn} \quad (1)$$

δ is the non-stoichiometry parameter which relates directly to the extent of the reduction step (oxygen release) and consequently its reverse oxidation (oxygen uptake). As stated in D2.1, in general $\delta \leq 0.5$ because for higher values the perovskite structure becomes unstable and as a direct result of this additional redox inactive phases may start to form.

The endothermic reduction comprises the charging step of the TCS scheme and oxidation is the discharging one. A high value of ΔH_{rxn} is desirable because this translates to a high (thermochemical) heat storage density while the targeted thermal boosting effect during discharge is magnified. Based on (1), it can be easily concluded that ΔH_{RXN} is directly proportional to δ, meaning that the higher the value of δ the higher the energy storage density becomes (see also D2.1).

A main challenge with the non-stoichiometric redox couples is that their occurrence is not defined by a specific equilibrium temperature as for the stoichiometric ones (e.g. Co_3O_4/CoO). Instead, their reduction is characterized by continuous oxygen release which starts above a certain temperature (700-750^{o}C for CMO-based compositions) and continues as long as the material is heated up (for ABSCPF the limit is 1100^{o}C). For the reverse oxidation, the reduced material starts to oxidize immediately upon its cooling. Thus, the two steps span a broad operating temperature range which, as described in D2.2 and D2.3, is in the range of 700-1100^{o}C. This broad range renders heat absorbance/ release during reduction/oxidation undetectable, most likely due to very slow evolution of the thermal phenomena. To validate and quantify these heat effects for at least one of the two reaction steps, a suitable operational protocol was devised and described in detail

in both D2.2 and D2.3. Based on this, a typical cycle involves reduction by heating up in air flow up to 1100°C, at atmospheric pressure, cooling in nitrogen flow down to lower temperature level and forced isothermal oxidation by switching back the flow from nitrogen to air while at the same time this air flow is fed pressurized (P_{air} = 1 – 6 bara). In this way, oxidation happens abruptly and heat release becomes detectable and measurable based on continuous temperature measurements both on the surface of the structured body and the temperature of air flow at the outlet of the structured body. This also corresponds to a clear thermal boosting effect (i.e. temperature increase during oxidation/stored chemical heat discharge), which can be identified and quantified.

Based on this protocol (with the exception of pressurization), a first quantitative estimation of the reaction enthalpies of redox reactions, associated with the qualified compositions of ABCSPF has been derived by DSC measurements of the corresponding powders, as analyzed in D2.2. Such DSC measurements during oxidation provided a first approximation of ΔH_{rxn}. The range was measured to be between ~ 99 $J \cdot g^{-1}$ and ~ 137 $J \cdot g^{-1}$ with the CMO composition exhibiting the highest value of this range. With these findings as basis and also acknowledging that shaped porous structures may actually differ from the DSC measurements performed on the respective powders at the mg-scale, the structured specimens of Table 1 were tested in the purpose built test-rig (Figure 1 and Figure 2). The protocols employed to identify the heat effects during oxidation were two:

- Protocol #1: The one as above mentioned to detect the oxidation-related heat effects.
- Protocol #2: one of a typical heat-up/cool-down (i.e. non-isothermal), under constant air flow and ambient total pressure in the range of the effective redox window of 700-1100°C, to assess continuous and repeatable reduction and oxidation but with no heat effects evident for this case.

Obviously, the quantified heat effects during oxidation via protocol #1 relate directly to ΔH_{rxn}. To be accurate, these actually correspond to an effective reaction enthalpy value ($\mathbf{\Delta H_{rxn,effective}}$) which can vary from one redox porous structure to another as explained later in the text. Additional heat-up/cool-down redox experiments (no isothermal oxidation) under constant air flow (and ambient total pressure) in the range of the effective redox window of 700-1100°C were also carried out as explained below.

The total number of cycles carried out per redox structure studied so far is provided in Table 2 below. These cycles refer to both protocols as explained above.

Structure	Total number of cycles carried out
CMO 59 cpsi honeycomb	72
CMO 111 cpsi honeycomb	80
CS10MO 59 cpsi honeycomb	203
CS10MO 60 ppi foam	214

Table 2: Total number of cycles carried out per redox structure (referring to both protocols)

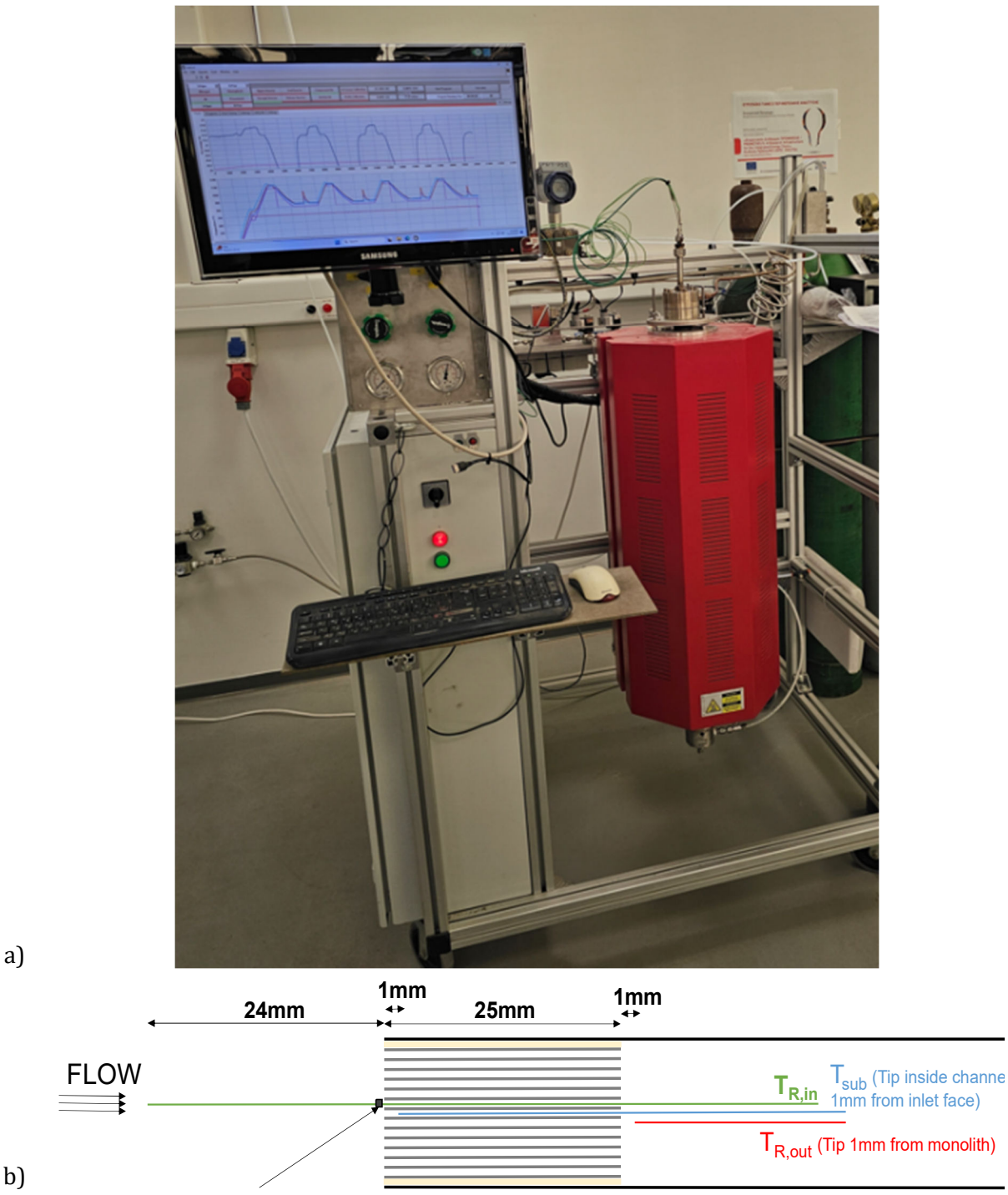

Figure 1: The purpose-built test-rig at CERTH: a) Photograph of the real unit, b) schematics of the indicative positioning of the 3 thermocouples employed for temperature measurements used for the calculation of heat effects (operation according to protocol #1) and shown for the case of a flow-through honeycomb structure in the reactor heated-up by the electrical furnace (red component in a). $T_{R,IN}$: the gas (air/nitrogen) temperature measured upsteam the redox structure; $T_{R,OUT}$: the gas (air/nitrogen) temperature measured downstream the redox structure; T_{SUB}: the temperature measured on the surface of the redox structure.

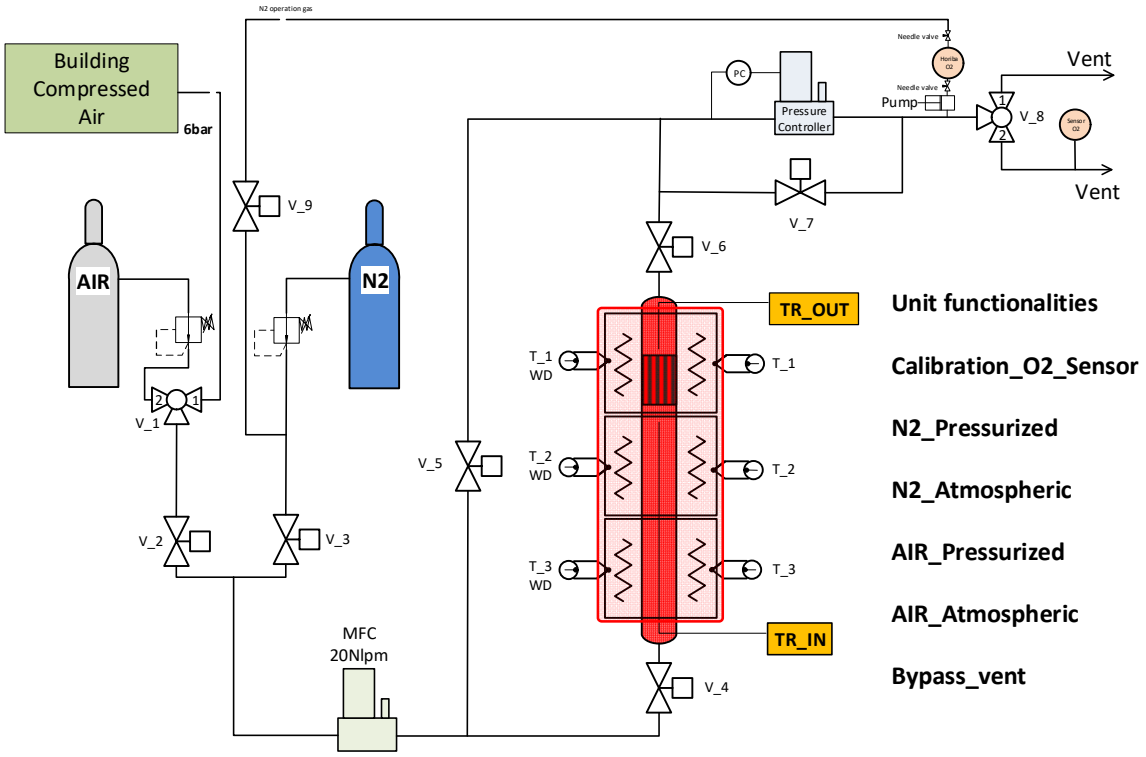

Figure 2: Simplified block diagram of CERTH's test-rig unit showing the main components such as the electrical furnace, the mass flow controller, the pressure controller, the thermocouples, the valves and the pressurized process gases.

2.1.1 Assessment of redox performance & comparative findings

The straightforward protocol #2 (see above) was used to directly validate the reversibility of the redox cyclic process. This is done by observing the cycle-to-cycle stability of oxygen released during reduction and consumed during oxidation and by also calculating and correlating the relevant amounts between the two steps both per cycle and overall (i.e. for the total number of cycles carried out according to protocol #2 in the frame of the multi-cyclic redox evaluation campaign). To put this into perspective, Figure 3 below shows an indicative and representative plot of the profiles of measured temperatures (see explanations in Figure 1) and oxygen concentration in the temperature range of 750 – 1100°C and continuous air flow (5 l·min^{-1} (std)) at atmospheric pressure as a function of the time of the experiment.

Evidently, the phenomenon is repeatable and the redox functionality is maintained throughout the 5-cycle redox experiment conducted. Similar profiles were derived for all 4 redox structures evaluated in the frame of their multi-cyclic performance assessment. The results/average values calculated in terms of normalized amount of oxygen produced/consumed and non-stoichiometry parameter (δ) during the cyclic process for the 4 structures tested so far are included in Table 3. Evidently, for a given structure there is good agreement between the amount of oxygen produced in reduction and consumed in oxidation, thereby proving the excellent reversibility of the cyclic scheme. By comparing the normalized amount of oxygen among the 4 redox structures assessed, it can be concluded that for a given structure geometry (59 cpsi honeycomb case) CS10MO performs much better than CMO (+25%). For a given composition (i.e. CMO), the 59 cpsi

honeycomb yields measurably more oxygen (+14%) than the 111 cpsi one. By comparing the foam with the honeycomb structure (CS10MO composition), both structures seem to be equally good.

By observing the profiles of the 3 temperatures measured, it is confirmed that, as mentioned earlier in the text, protocol #2 fails to identify the effect of endothermic and exothermic phenomena on the temperature measurements. Both the temperature of the substrate (TR_{SUB}) and the air flow downstream the redox structure (TR_{OUT}) simply follow the heating-up/cool-down program of the electrical furnace, they coincide with each other to a large extent and there are no identifiable heat effects in the course of the oxygen concentration variations recorded.

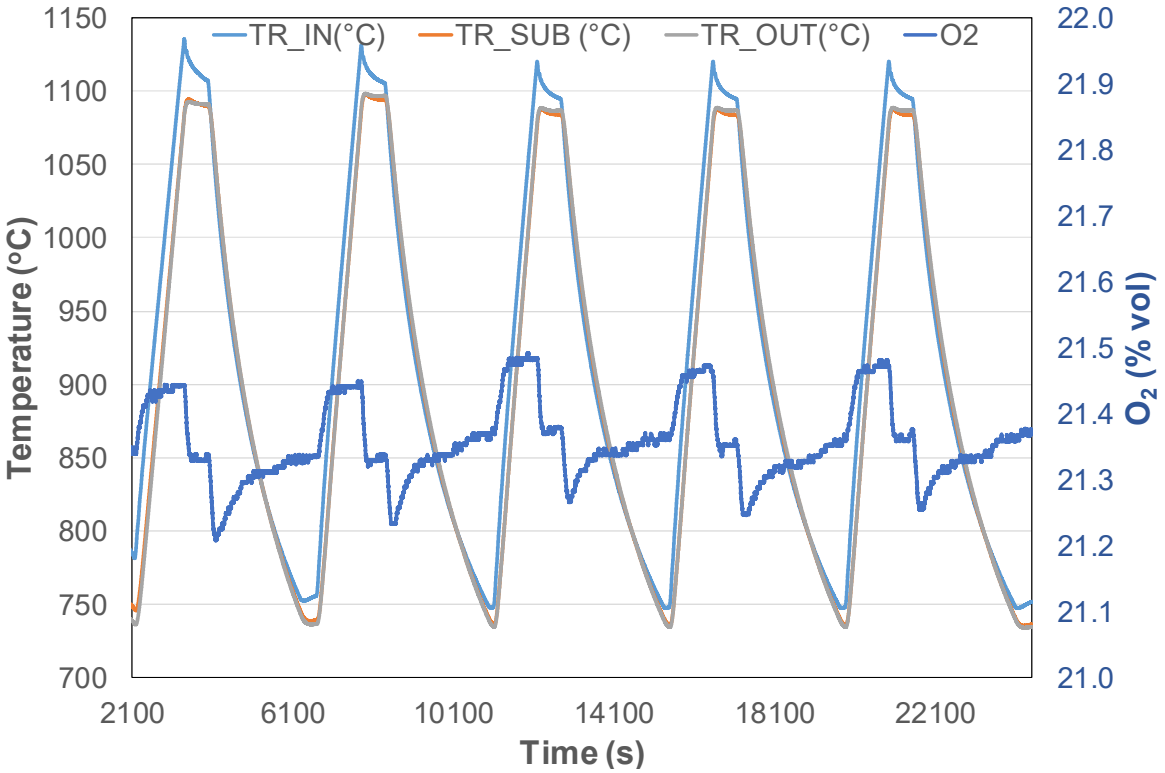

Figure 3: Representative profile of a 5-cycle redox experiment carried out with the CS10MO 60 ppi foam according to protocol #2. TR_IN: the air flow temperature measured upsteam the redox structure; TR_OUT: the air flow temperature measured downstream the redox structure; TR_SUB: the temperature measured on the surface of the redox structure.

Structure	O_2 produced during reduction in mmol/g (average)	O_2 consumed during oxidation in mmol/g (average)	δ (average)
CMO 59 cpsi honeycomb	0.335 ± 0.033	0.310 ± 0.023	0.096 ± 0.009
CMO 111 cpsi honeycomb	0.297 ± 0.063	0.286 ± 0.032	0.084 ± 0.018
CS10MO 59 cpsi honeycomb	0.414 ± 0.015	0.399 ± 0.016	0.118 ± 0.004
CS10MO 60 ppi foam	0.391 ± 0.035	0.380 ± 0.041	0.116 ± 0.010

Table 3: Overview of average amounts of oxygen released/consumed during the multi-cyclic evaluation campaigns (according to protocol #2) of the 4 redox structures tested so far

2.1.2 Evaluation of energetic performance and comparative assessment

The energetic performance of the redox structures studied so far is based on the calculated energy density as derived from the sum of their sensible heat storage capacity corresponding to the 300-1100ºC operating temperature range defined in the project's DoW and the contribution of their TCS component. For a given material composition, a certain packed (bulk) density and a specific operating temperature range, the sensible heat potential is constant and straightforwardly calculated. On the other hand, the TCS energy density relates to several parameters that directly or indirectly affect the oxidation reaction and thus it may vary considerably per set of operating parameters under which the chemical phenomenon occurs. Thus, the present paragraph emphasizes on the TCS part per redox structure (denoted in the text as E to be consistent with the submitted deliverable D2.3). In paragraph 2.1.4, the two energies are summed up to provide the total potential of energy storage density per case and the assessment against the relevant KPI requirement of the project (i.e. > 300 kWh·m^{-3}).

A typical indicative experiment carried out according to protocol #1 for the case of the 59 cpsi CS10MO honeycomb and showing clearly the heat effects of the oxidation reaction is provided in Figure 4 below. For all 4 structures studied so far, the relevant pro-

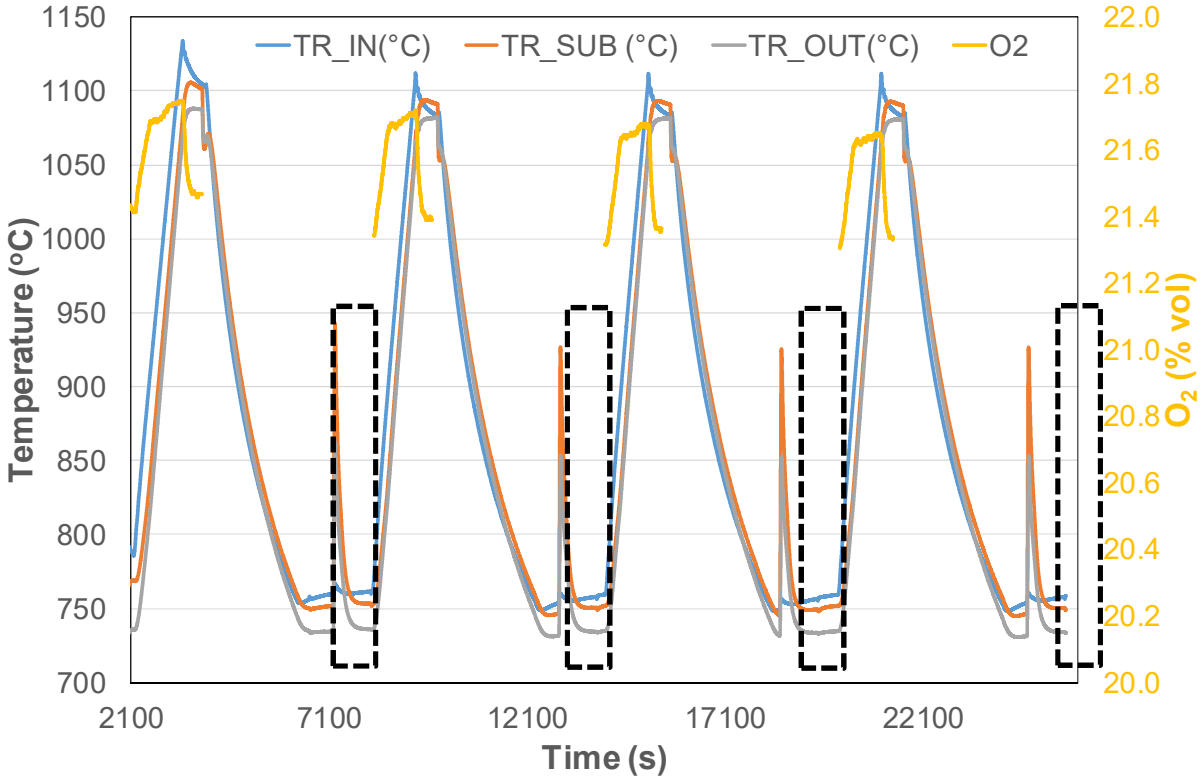

Figure 4: Representative profile of a 4-cycle redox experiment carried out with the CS10MO 59 cpsi honeycomb according to protocol #1 at the oxidation temperature at 750ºC and total pressure (P_{TOT}) of 6 bara. TR_IN: the air flow temperature measured upsteam the redox structure; TR_OUT: the air flow temperature measured downstream the redox structure; TR_SUB: the temperature measured on the surface of the redox structure. During this operational mode O_2 measurement is possible only during the reduction step.

files are qualitatively identical. This means that in all cases, the experimental validation of temperature boosting (i.e. sharp temperature increase) from the beginning to the end of the oxidation reaction is evident and follows a profile as shown in the representative plot below (see marked areas). This important temperature boosting effect is solid proof for the validity of the project's core concept and appears both in the temperature of the structure (increase in T_{R_SUB}) and in the temperature of the air flow downstream the structured body (increase in T_{R_OUT}). As expected, T_{R_IN} remains unaffected by the exothermal phenomenon. Observing the 4 oxidation steps indicated/marked in Figure 4 as well as the oxygen profiled recorded during the preceding reduction step, it is evident that there is good cycle-to-cycle repeatability.

$\Delta H_{rxn,\,effective}$ (equivalent to E as explained earlier in the text) is based on the T_{R_SUB} measurements in the course of the oxidation reaction and is calculated as follows:

$$E = \Delta H_{rxn,effective} = \sum_{to}^{tf} m_{SUB} \cdot Cp_{SUB} \cdot dT_{R\_SUB} \qquad (2)$$

where m_{SUB} is the mass of the porous structured body, Cp_{SUB} is the specific heat capacity of the material (see deliverable D3.1 for corresponding average values) and dT_{R_SUB} is the absolute value of the instantaneous temperature difference on the surface of the structured body at any given time in the course of the oxidation evolution; with start time of the reaction at **to** and completion time at **tf**.

Based on the whole set of experiments carried out for the 4 redox structures studied so far and the methodology for ΔH_{rxn} stated above, the corresponding thermochemical energy densities can be calculated. Table 4 provides an overview of effective reaction enthalpies per structure for 3 different oxidation temperatures. In the next paragraph, detailed correlations of ΔH_{rxn} with both oxidation temperature and pressure for the entire studied range of the latter two parameters are provided.

Structure	$\Delta H_{rxn,effective}$ at $T_{oxidation}$ = 750°C (J·g^{-1})	$\Delta H_{rxn,effective}$ at $T_{oxidation}$ = 900°C (J·g^{-1})
CMO 59 cpsi honeycomb	347	262
CMO 111 cpsi honeycomb	296	182
CS10MO 59 cpsi honeycomb	495	410
CS10MO 60 ppi foam	528	393

Table 4: Calculated $\Delta H_{rxn,effective}$ values at 2 indicative oxidation temperatures and oxidation pressure of 6 bara for all 4 porous redox structures tested so far

A clear first conclusion is that the CS10MO composition is considerably superior to CMO in terms of thermochemical energy density potential. Moreover, by comparing the geometries for a given composition, the 59 cpsi honeycomb is better for the CMO while for CS10MO the honeycomb and the foam are equally good in terms of thermochemical heat storage potential per unit mass. However, considering that the bulk/packing density of the 59 cpsi honeycomb is approximately 2.6 times higher than that of the foam (Table 1), the honeycomb structure has a significant advantage in terms of volumetric energy density potential. Thus, the 59 cpsi CS10MO honeycomb is the preferred choice for consideration and further details on the correlation of the main performance metrics of

the ABCSPF redox scheme with important operating parameters of interest are analyzed and provided in detail in the next paragraph for this specific optimized case.

2.1.3 Extracted correlations between redox & energetic performance parameters and operating conditions

The present paragraph contains correlations between the effective reaction enthalpy ($\mathbf{\Delta H_{rxn,effective}}$) and the most important operating parameters, as identified by the experimental studies carried out so far. **These correlations were extracted from the multi-cyclic campaign of the 59 cpsi CS10MO honeycomb**, which – as already explained above – is clearly the best one in terms of its calculated energy density among the formulations studied until the time of submission of the present deliverable.

As explained earlier in the text, it is practically impossible to measure experimentally the intrinsic reaction enthalpy (ΔH_{rxn}) of the redox reaction. With the aid of the experimental campaigns of WP3, the heat effects identified and quantified via temperature measurements on the surface of the redox structure during isothermal oxidation can be considered as a reliable measure of the apparent reaction enthalpy, which is essentially an effective value that provides the extra heat added to the system via the exothermal (oxidation/chemical discharging) reaction step. The value of $\Delta H_{rxn,effective}$ varies with:

a) the oxidation temperature (TR_SUB value in the isothermal step before oxidation in Figure 1),

b) the extent of the reduction (charging step) of the redox structure that precedes the oxidation (discharging) step to close the cycle. An equivalent parameter for this is the non-stoichiometry factor (δ),

c) the total pressure of air /partial O_2 pressure during the (isothermal) oxidation.

Below, relevant Figures (4 through 7) and extracted apparent correlations are provided. It should be noted that, in general, these correlations are relatively safe for use within the range of the independent parameters addressed per case and any extrapolation outside of this range should be done with caution. It must be noted that with the exception of $\Delta H_{rxn,effective}$ vs δ, the extracted correlations are linear and the correlation coefficient (R^2) varies between 0.76 and 0.99, thereby indicating very good fitting with the experimental data. The main observations are:

- The extent of reduction reaction, as indicated by δ, increases monotonically with the temperature and at 1100°C the non-stoichiometry factor reaches a value of approximately 0.12 (Figure 5). This is in good agreement with the previously calculated δ values in deliverables D2.2 and D2.3.
- The value of $\Delta H_{rxn,effective}$ decreases as the oxidation temperature increases and the dependence is clearly linear in the broad temperature range of 700-1000°C studied (Figure 6). Reaction enthalpy dropped by approximately 35% from 700 to 1000°C, which indicates a clear – yet not very profound – decrease. Even at 1000°C, the reaction heat effect remains substantial.

- Obviously, the higher the value of δ during reduction the higher the value of $\Delta H_{rxn,effective}$ in the course of the subsequent oxidation step (Figure 7).
- At any given oxidation temperature studied, pressurized oxidation has a measurable, yet not very profound, positive effect on $\Delta H_{rxn,effective}$ (Figure 8). The apparent/effective reaction enthalpy increases in a near-linear trend and the slope per oxidation temperature is similar. A deviation from linearity is observed at high oxidation temperature (i.e. 900 and 1000°C). For these two temperatures, $\Delta H_{rxn,effective}$ seems to reach a plateau already at P_{air} = 3 bara, as further increase in the oxidation pressure to 6 bara causes only a marginal increase in $\Delta H_{rxn,effective}$.

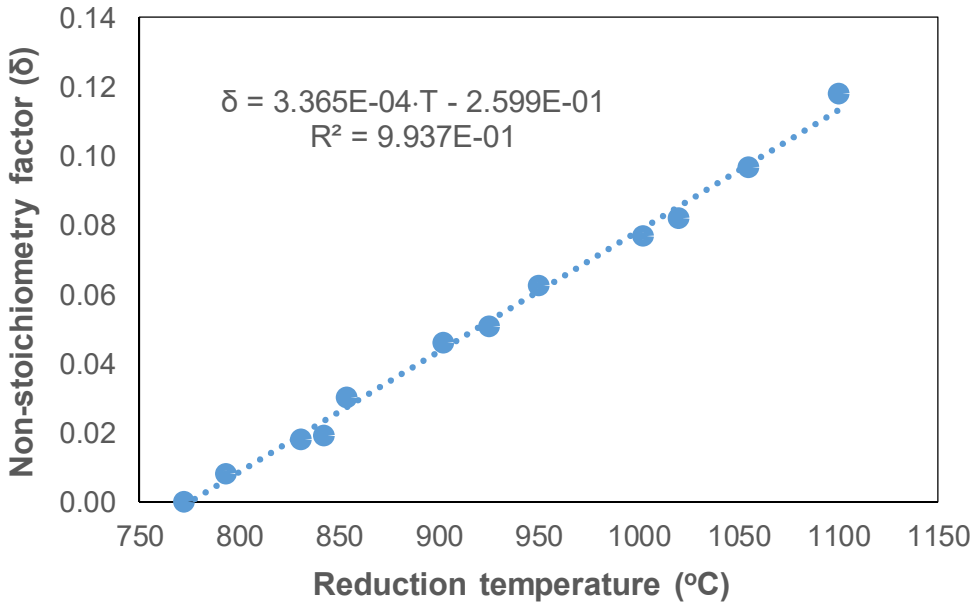

Figure 5*:* Dependence of δ on the reduction temperature at P_{air}= 1 bara and the extracted linear fitting of the experimental data. The correlation should be used for reduction temperature - $T_{reduction}$ > 800°C.

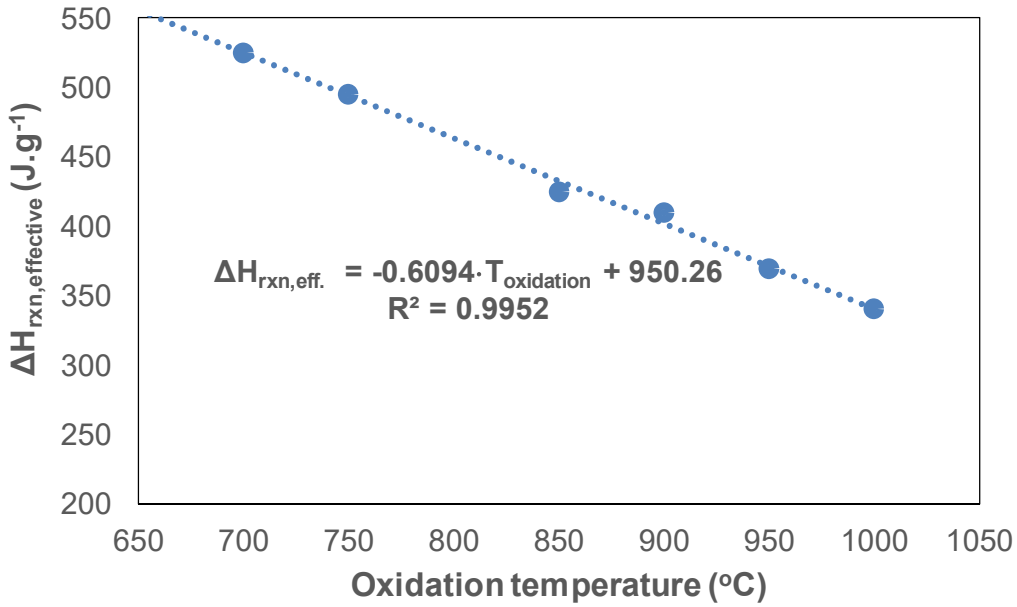

Figure 6*:* Dependence of $\Delta H_{rxn,effective}$ on the oxidation temperature at P_{air} = 6 bara and extracted linear fitting of the experimental data.

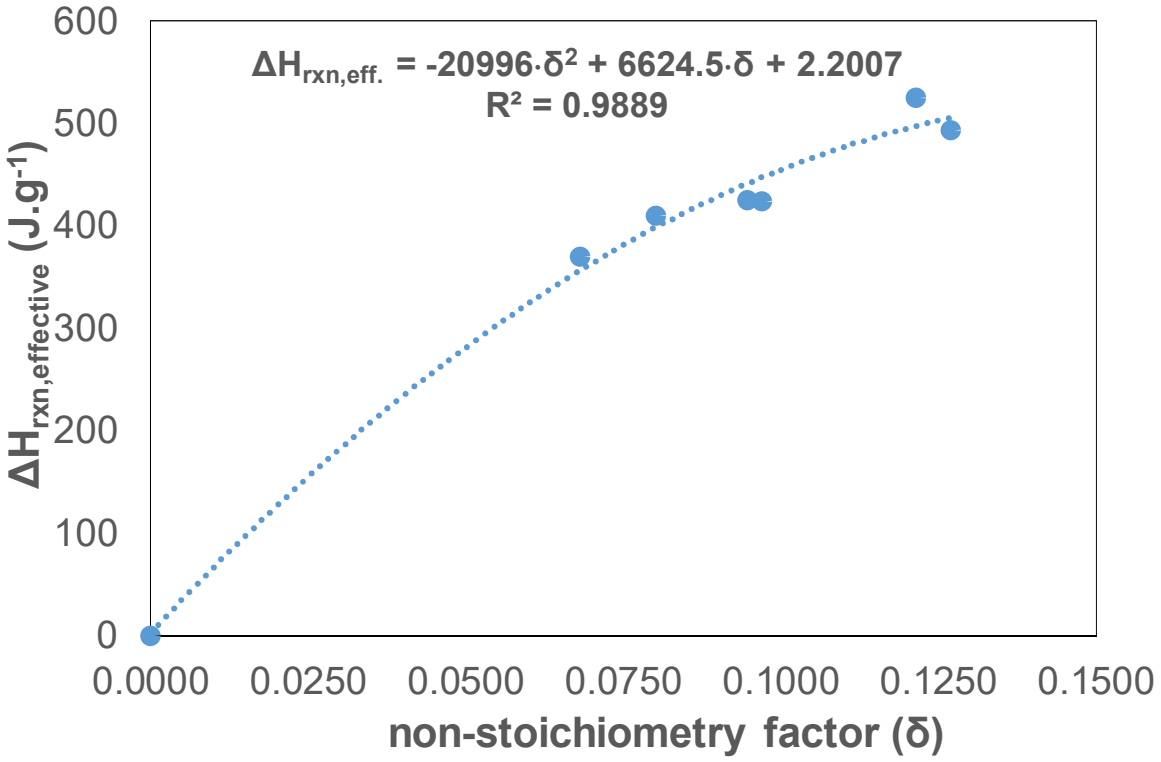

Figure 7*:* Dependence of $\Delta H_{rxn,effective}$ on the value of δ and extracted polynomial fitting of the experimental data.

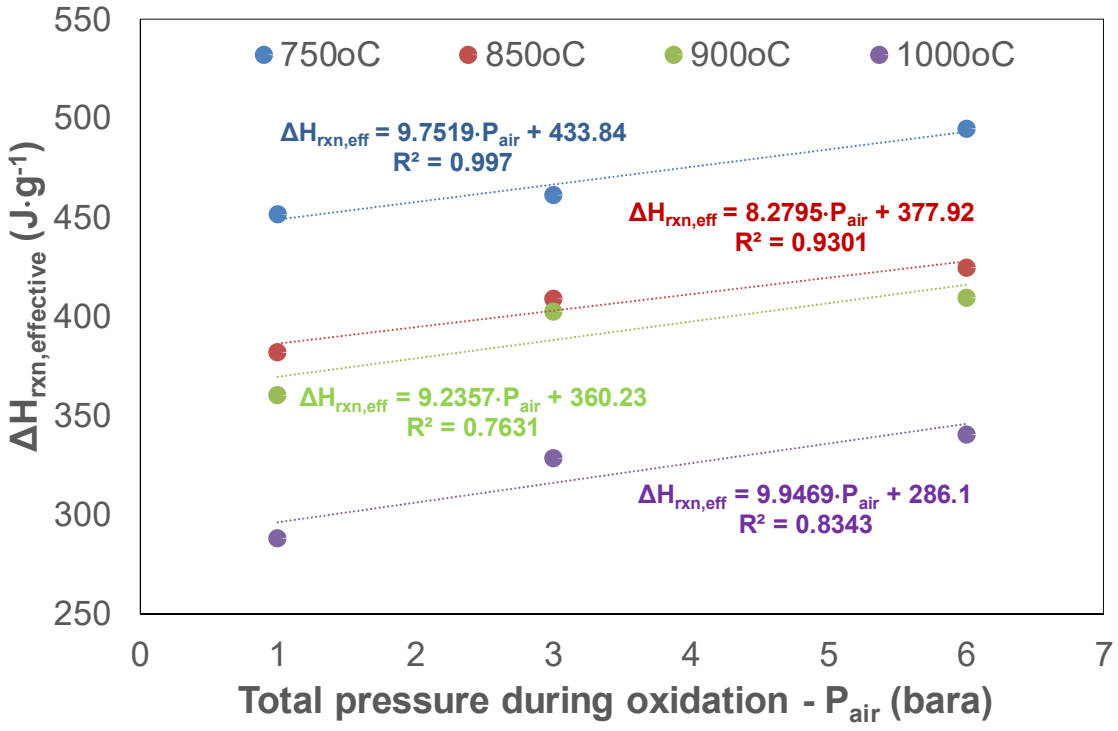

Figure 8*:* Dependence of $\Delta H_{rxn,effective}$ on the total air pressure (P_{air}) during (isothermal) oxidation at four different oxidation temperatures in the range of 750-1000°C.

The oxidation of the redox structure results to **a clear and substantial thermal boosting effect** caused by the exothermal reaction, as first demonstrated by the experimental results shown in Figure 4. In practice, this thermal boosting effect is assessed

in the form of the measured temperature increase in the air outlet flow (i.e. air flow downstream the honeycomb) in the course of the isothermal oxidation operation mode. Figure 9 below presents both the maximum value of recorded temperature increase in the air outlet flow during oxidation (i.e. $\Delta T_{air,max}$) and the maximum value of recorded temperature increase on the surface of the honeycomb (substrate) during the same reaction step (i.e. $\Delta T_{SUB,max}$). The latter is also provided because it refers to the absolute maximum achievable thermal boosting effect, assuming a perfect solid-gas heat exchange process at a hypothetical gas-solid thermal equilibrium state. Fitting linear equations (dotted lines) are also provided. Evidently, the thermal boosting effect shows a monotonic decrease with the oxidation temperature. This is in full agreement/closely related to the trend already presented and commented upon in Figure 6. **In all cases, the thermal boosting effect is substantial; air flow temperature increases by 76 to 140°C while – as expected – the effect of the substrate temperature is more profound and the boosting is in the range of 133-206°C.** For the entire oxidation temperature range studied, the gap between the two curves (i.e. $\Delta T_{SUB,max}$ and $\Delta T_{air.max}$) is approximately constant at ~60°C.

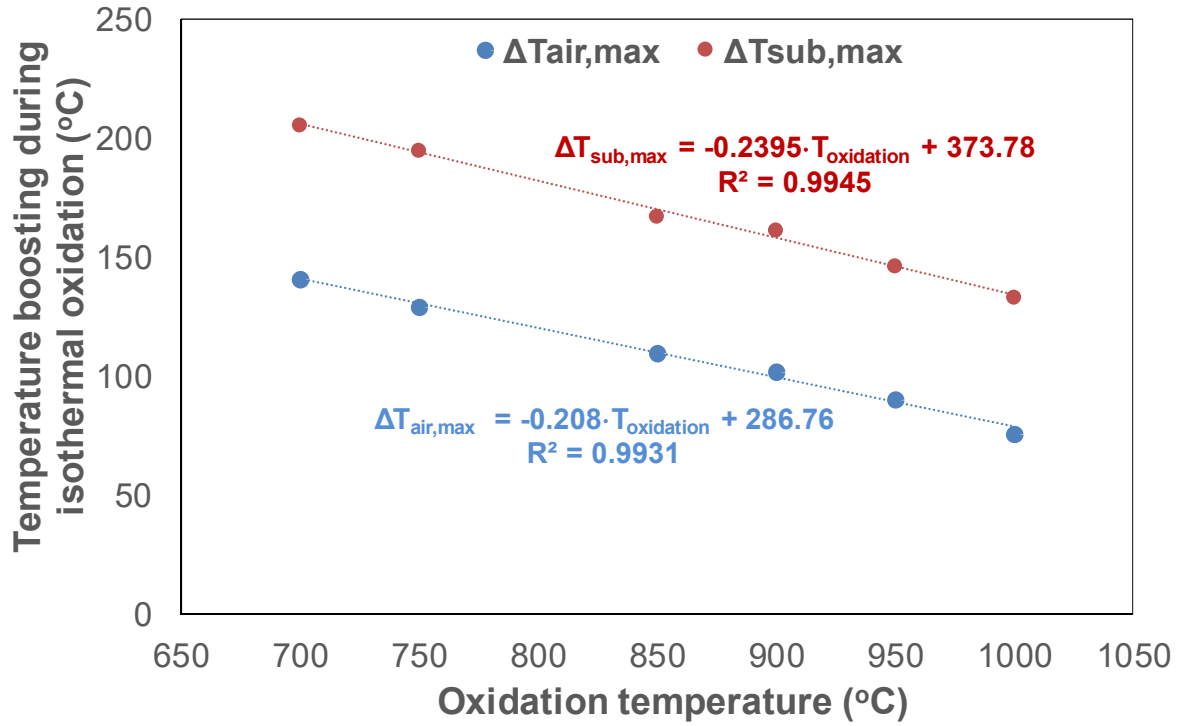

Figure 9*:* Temperature boosting (ΔT) of both air flow at the outlet of the redox honeycomb and on the substrate as a function of the substrate oxidation temperature (operation mode as shown in Figure 1). P_{air} = 6 bara.

It must be stressed that the above apparent correlations using experimental data of the redox system constitute **valuable input to WP4 studies**, which is thus directly exploitable therein to setup the necessary storage reactor model at first and subsequently carry out the overall system simulation studies.

2.1.4 Total energy density of redox structures, redox stability assessment and evaluation against the energy density target of project's milestone M2

As already explained in deliverable D2.3, the total energy density potential (Q_{total}) of the hybrid sensible/thermochemical heat storage medium (here referring to structured redox bodies) for the targeted 300-1100°C operating temperature range is calculated as:

$$Q_{total} = d_{bulk} \cdot (C_p \cdot \Delta T + E) \cdot 1/3.6 \qquad (3)$$

Where d_{bulk} is the bulk/packing density of structures as indicated in Table 1, Cp is the specific heat capacity of either CMO or CS10MO as provided in deliverable D2.3, ΔT = 800 K (i.e. corresponding to the 300-1100°C temperature range), $E = \Delta H_{rxn,effective}$ (see Table 4) and 1/3.6 is the conversion factor from J/ml to kWh/m³. Table 5 includes the calculated Q_{total} values for all 4 redox lab-scale structures evaluated so far as well as the calculated % contributions of the sensible heat and thermochemical heat storage components. Evidently, sensible heat storage contribution is dominant however the thermochemical one is also appreciable in all cases. In the case of CS10MO composition and in particular for the foam formulation, the thermochemical contribution is higher.

Structure	Q_{total} (in KWh/m³)	% Sensible / % Thermochemical
CMO 59 cpsi honeycomb	**800**	73 / 27
CMO 111 cpsi honeycomb	**405**	84 / 16
CS10MO 59 cpsi honeycomb	**840**	68 / 32
CS10MO 60 ppi foam	**350**	64 / 36

Table 5: Calculated Q_{total} values for the 4 redox lab-scale structures studied so far

Based on the values above, which are all clearly above 300 kWh/m³, it can be concluded that **there is sufficient experimental proof for the successful fulfilment of the energy density requirement of project's milestone M2, which refers to the specific target of combined *TCS + sensible energy density ≥ 300 kWh/m³***.

The redox performance stability of the structures can be assessed in a straightforward manner by the profiles of their reduction/oxidation in the course of their multi-cyclic campaigns. For brevity, Figure 10 contains only the profiles referring to the 59 cpsi CS10MO honeycomb. These are, however, representative to all 4 cases studied as the respective results from all the other 3 are qualitatively identical to the plots included in Figure 10 **meaning that all structures showed remarkable cycle-to-cycle stability**. Note that the oxidation graph in Figure 10 contains a substantially lower number of measurements cf. the one for reduction due to the fact that, as explained earlier, oxygen cannot be recorded during experiments carried out according to protocol #1. Thus, only exploitable measurements from protocol #2 are included, which however refer to cycles with a distribution throughout the entire 203-cycle campaign.

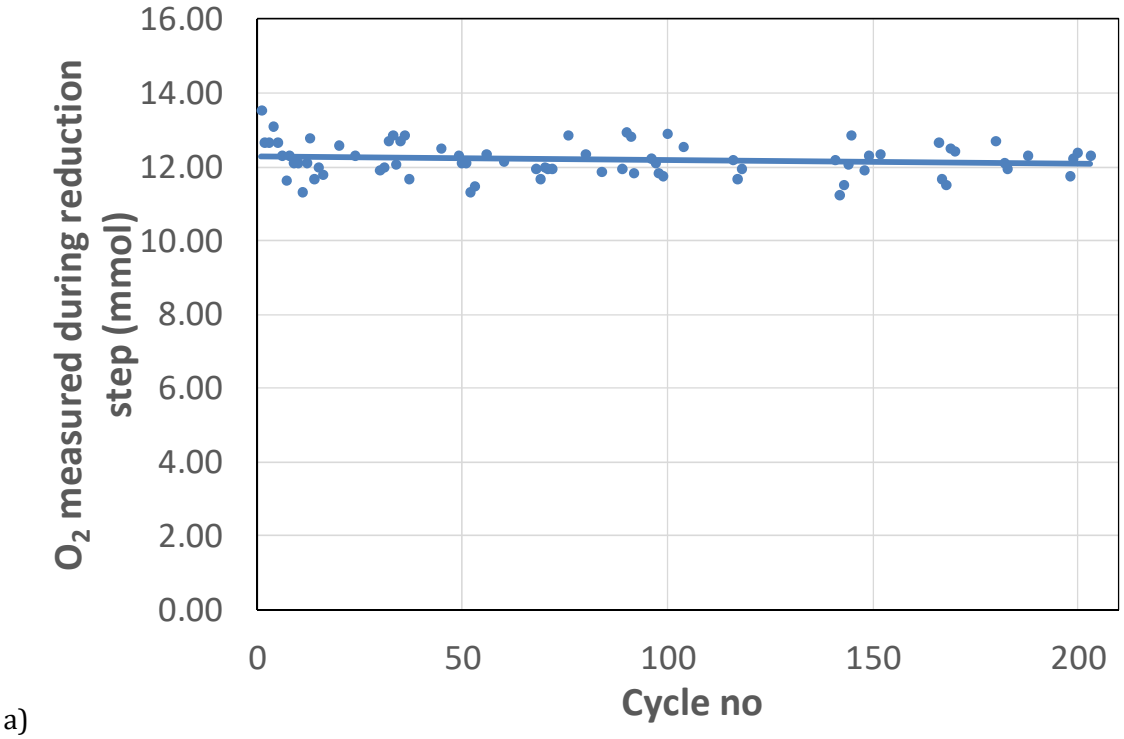

a)

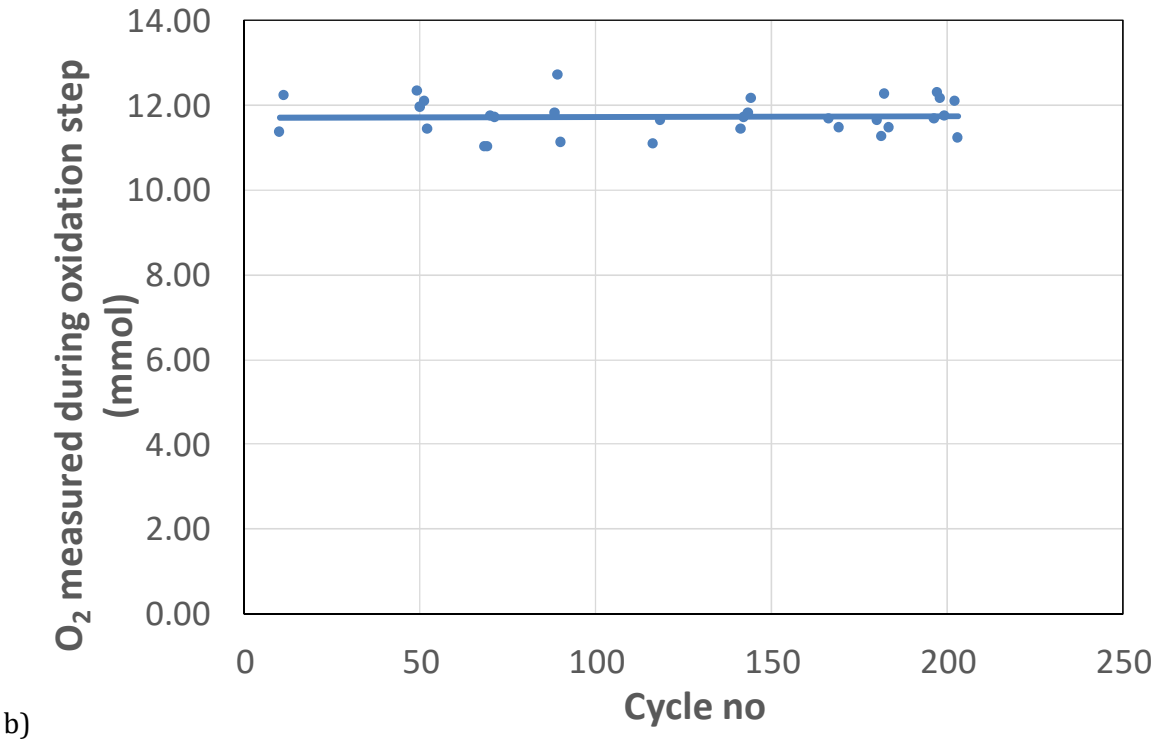

b)

Figure 10*:* Oxygen profiles of the 59 cpsi CS10MO honeycomb, as extracted from the 203-cycle campaign: a) oxygen produced during the reduction step vs the cycle number (measurements from both protocol #1 and #2); b) oxygen consumed during the oxidation step (measurements possible with protocol #2 only).

3. Mechanical and thermomechanical evaluation of redox structures and comparison with reference ones

The present section refers to measurements and analyses that relate to the robustness of the prepared structures and their resilience to the imposed high temperature thermal-thermochemical process. Crushing strength measurements include results from pristine lab-scale redox structures and how these compare to similar reference structured bodies made of inert materials (i.e. cordierite), thereby proving that the structures studied are sufficiently robust, at least in the as-produced/ready-to-use form. The first measurements to directly compare pristine structures and their respective counterparts after > 200 cycles have already been scheduled. Based on comparative structural, morphological and textural findings (via both visible or macroscopic observations/measurements, microscopy and additional analyses) the first clear conclusions are extracted and, pending some additional measurements currently scheduled to be completed by end of February 2025, there is already clear evidence that the 59 cpsi CS10MO honeycomb structure is robust enough to withstand multi-cyclic (> 200 cycles) high temperature redox operation, as required by the targeted ABCSPF application.

3.1 Crushing strength measurements

Representative porous structured specimens, namely honeycombs and foam-like bodies prepared out of the Sr-doped calcium manganite reference compositions of the project, CMO, C95S5MO and C90S10MO as well as a first set of honeycombs made of non-redox-active, recycled materials (see D3.1) were tested at DLR with respect to their compressive (crushing) strength in comparison to “reference” commercial, non-redox cordierite honeycomb specimens. Specimens of the commercial structures were core-drilled from larger, commercial-size pieces of the respective cpsi.

Table 6 lists the tested specimens with their composition, pore structure properties (cpsi, ppi for the honeycombs and the foams respectively) their sintering temperature, dimensions and weight. The table also lists the calculated “envelope” densities (i.e. mass of the specimen divided by its external “geometrical” volume) and their porosity and mean pore diameter measured by mercury (Hg) porosimetry on specimens of the same specifications and prepared under the same conditions (since the specimens needed for mechanical strength tests had to be integral parts without any piece removed from them for porosity measurements), as reported in D3.1(measurements to determine the values currently missing from the table are ongoing). These two properties, together with the “density” of the microstructure (i.e. higher or lower ppi/cpsi number) are directly correlated to the mechanical strength of the specimens. Based on the specimens’ production and availability, only one specimen per type of in-house extruded honeycombs by CERTH and three (3) specimens from each commercial structure and

from in-house produced foams by DLR were used in the measurements. The results for the last two cases were reproducible from specimen to specimen; therefore, the table and the relevant following figures include only one typical specimen from each of these categories, for reasons of clarity.

The first set of crushing strength tests on commercial cordierite honeycombs and on in-house prepared foams was performed with an Instron universal testing machine model 5566A having a maximum load capacity of 10 kN, with compression rate 1 mm/min. The machine is equipped with a set of two different cameras, one connected directly to it so that the acquired still photos every ca. 0.025 sec are synchronized with the applied load and one external, to record the whole experiment for visual observation. Alumina fleece pieces were placed on top and bottom of each sample to ensure a more uniform force distribution. However, as will be described below, the strength of the in-house made honeycombs was so high that it was impossible to crush them applying the specific maximum load (10 kN). Therefore, another device with a maximum load capacity of 100 kN was employed to crush these specimens, which, however, did not have the option for a "synchronized-to-the-load camera" and hence these experiments were recorded only with the external camera. Photos of each type of specimen on the testing device(s) at the beginning of each experiments are shown in Figure 11. It should be noted that the lower plate of the press of the instrument capable of applying the higher load is moving, in contrast to the first instrument where the upper one does; hence the difference in the photographs (a)-(c) and (d)-(e) of the figure.

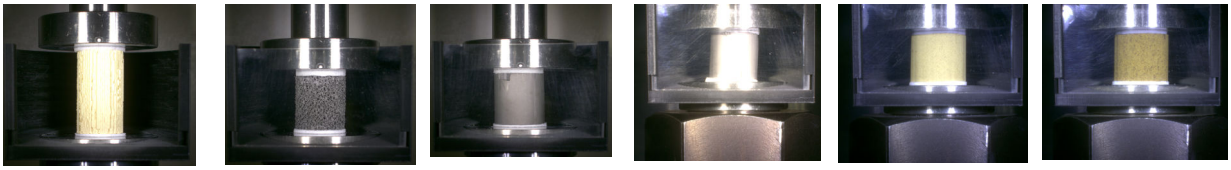

(a) (b) (c) (d) (e) (f)

Figure 11: The five categories of tested specimens, placed on the mechanical testing device(s) fefore start of experiments: (a) commercial cordierite honeycomb, (b) in-house made CMO foam and (c) in-house made CMO honeycomb on testing device with maximum compressive load of 10 kN; (d), (e), (f) in-house made CMO, A4 and BM/B honeycombs, respectively, on testing device with maximum compressive load of 100 kN.

It has to be stressed that all such honeycomb and foam structures like the ones tested here, are highly anisotropic, hence the crushing (compressive) strength tests reveal and compare their performance only along the longitudinal axis. Furthermore, they are all highly porous structures with a high percentage of void area – the so-called "open frontal area" - occupying their cross-section; this "open frontal area" is comprised by the total area of the square-shaped channels in the case of honeycombs or the area of the quasi-spherical mega-pores defined by the struts' walls in the case of foams. In the results and graphs that follow, the compressive stress in MPa is calculated by dividing the applied load with the total area of the circular cross-section of the cylindrical specimens, and not by the actual area of the solid within this cross-section that actually bares the load.

Composition	Sample Type	PPI/ CPSI	D (mm)	Mass (g)	Sintering Temperature (°C)	Volume (cm^3)	Envelope Density (g/cm^3)	Hg porosimetry	
								Porosity (%)	Mean pore diameter (µm)
CS10MO	Foam	30	25.48	8.57	1200	12.75	0.67	46	21
CS10MO	Foam	30	24.64	9.03	1300	11.92	0.76	40	19
CS10MO	Foam	60	25.70	9.02	1200	12.97	0.70	58	49
CS10MO	Foam	60	24.87	9.31	1300	12.14	0.77	31	89
CS5MO	Foam	30	25.93	9.88	1200	13.20	0.75	scheduled	scheduled
CS5MO	Foam	30	24.19	11.51	1300	11.49	1.00	scheduled	scheduled
CS5MO	Foam	60	25.48	10.14	1200	12.75	0.80	scheduled	scheduled
CS5MO	Foam	60	23.64	11.12	1300	10.97	1.01	scheduled	scheduled
CMO	Foam	30	25.52	9.47	1200	12.78	0.74	scheduled	scheduled
CMO	Foam	30	23.96	10.96	1300	11.27	0.97	scheduled	scheduled
CMO	Foam	60	25.53	10.36	1200	12.80	0.81	scheduled	scheduled
CMO	Foam	60	24.05	11.33	1300	11.36	1.00	scheduled	scheduled
Cordierite 1	Honeycomb	400	23.03	2.78	-	10.41	0.27	34	6.2
Cordierite 2	Honeycomb	600	22.99	3.52	-	10.38	0.34	31	6.6
Cordierite 3	Honeycomb	900	22.97	2.99	-	10.36	0.29	26	1.6
A4	Honeycomb	44	29.18	19.86	1250	16.71	1.19	32	1.17
BM/B	Honeycomb	44	29.73	17.34	1250	17.35	1.00	51	6.94
CS10MO	Honeycomb	44	25.90	29.09	1300	13.17	2.21	25	1.10
CMO	Honeycomb	44	26.35	28.21	1300	13.63	2.07	27	1.36
CMO	Honeycomb	90	25.98	15.37	1300	13.25	1.16	25	1.30

Table 6: Types and characteristics of specimens subjected to crushing strength tests.

The results from the in-house made foams are summarized in Figure 12. Maximum compressive strength values vary between 1-3.5 MPa, depending on composition, sintering temperature and ppi. Qualitatively, in almost all cases, the point of maximum compressive strength is not followed by a sharp decrease of the compressive stress and does not seem to be a distinct point of terminal failure; it most likely corresponds to fracture of the weakest struts initiated perhaps at possible pre-existing flaws. Nevertheless, the foam does not "break" at this point but continues to deform as more and more struts break one after the other, until eventually it collapses completely. As expected, foams of the same composition and ppi sintered at the higher temperature exhibit higher maximum crushing strength than that of their counterparts sintered at the lower temperature of 1200ºC; this latter temperature seems not sufficient to induce satisfactory mechanical strength of the foams, hence sintering of foams at least at 1300ºC is recommended. Among foams of the same composition and sintered at the same temperature these of higher ppi exhibit also higher maximum strength.

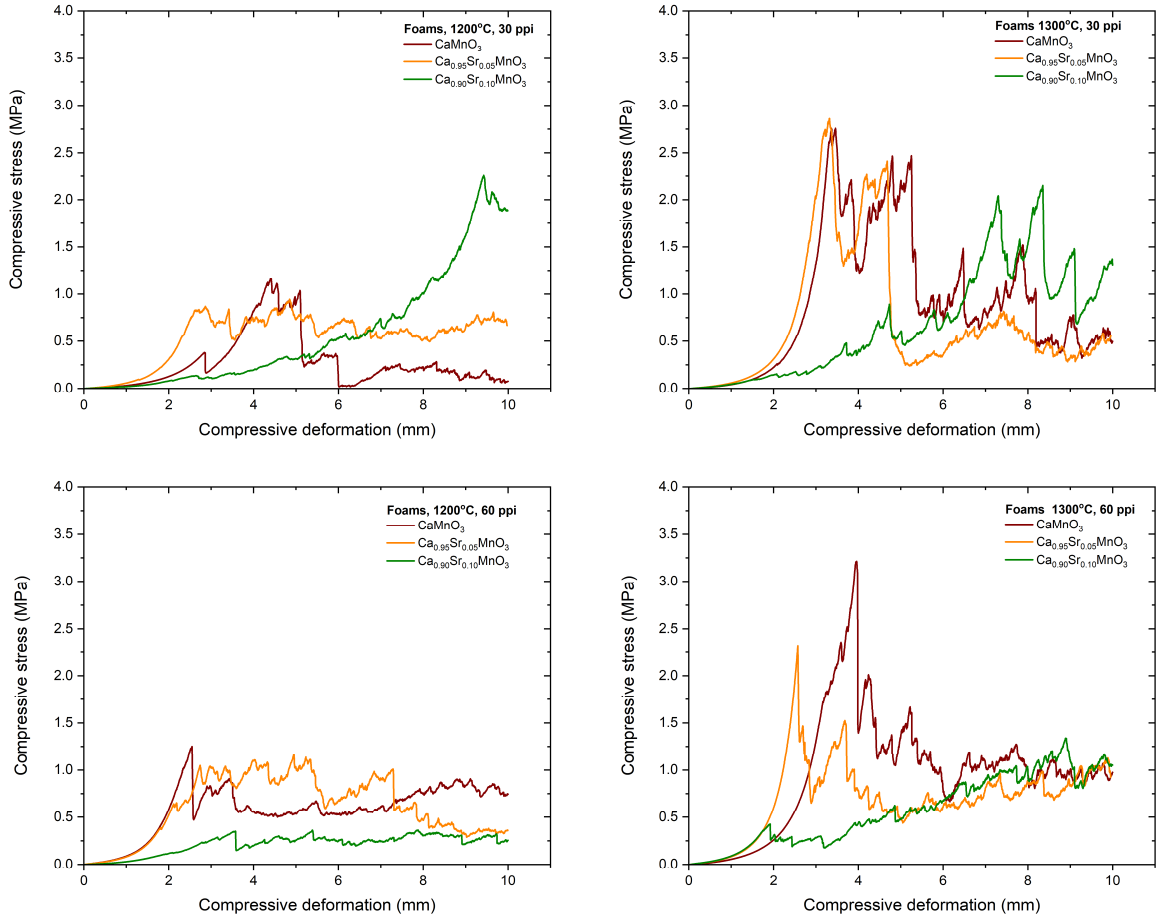

Figure 12: Compressive stress-deformation curves of in-house produced foam specimens as a function of Sr-dopant in the A-site (curves of different colour), sintering temperature (left column: sintered at 1200ºC, , right column: 1300ºC) and "structural" density (top row: 30 ppi, bottom row: 60 ppi).

The effect of Sr dopant seems less straightforward: whereas the curves corresponding to CMO (brown lines) and CS5MO (orange lines) look qualitatively and quantitatively similar for every sintering temperature and ppi, the ones of CS10MO (green

lines) look substantially different. In both sintering temperatures, doping with 10 atomic (at) % Sr shifts the peak of the compressive strength to higher deformations - case of the 30 ppi foams - or eliminates such peaks completely - case of 60 ppi foams. The effect of ppi becomes very different in the CS10MO foams in contrast to the CMO and the CS5MO ones. This observation supports the idea, substantiated by the results of other experiments that addition of Sr beyond a critical concentration threshold – (ca. 10 %) - changes significantly several phase transformations, lattice parameters and relevant thermal and mechanical properties. Experiments with more specimens per composition as well as with compositions of higher Sr (e.g. 20 at %) are scheduled to try to shed light on this issue.

The results from the in-house extruded honeycombs, perovskite and redox-inactive, are shown in Figure 13 in comparison to those of commercial cordierite ones. As already mentioned the specific perovskite honeycombs could not be crushed with a maximum load of 10 kN and a load of 100 kN was employed for that purpose.

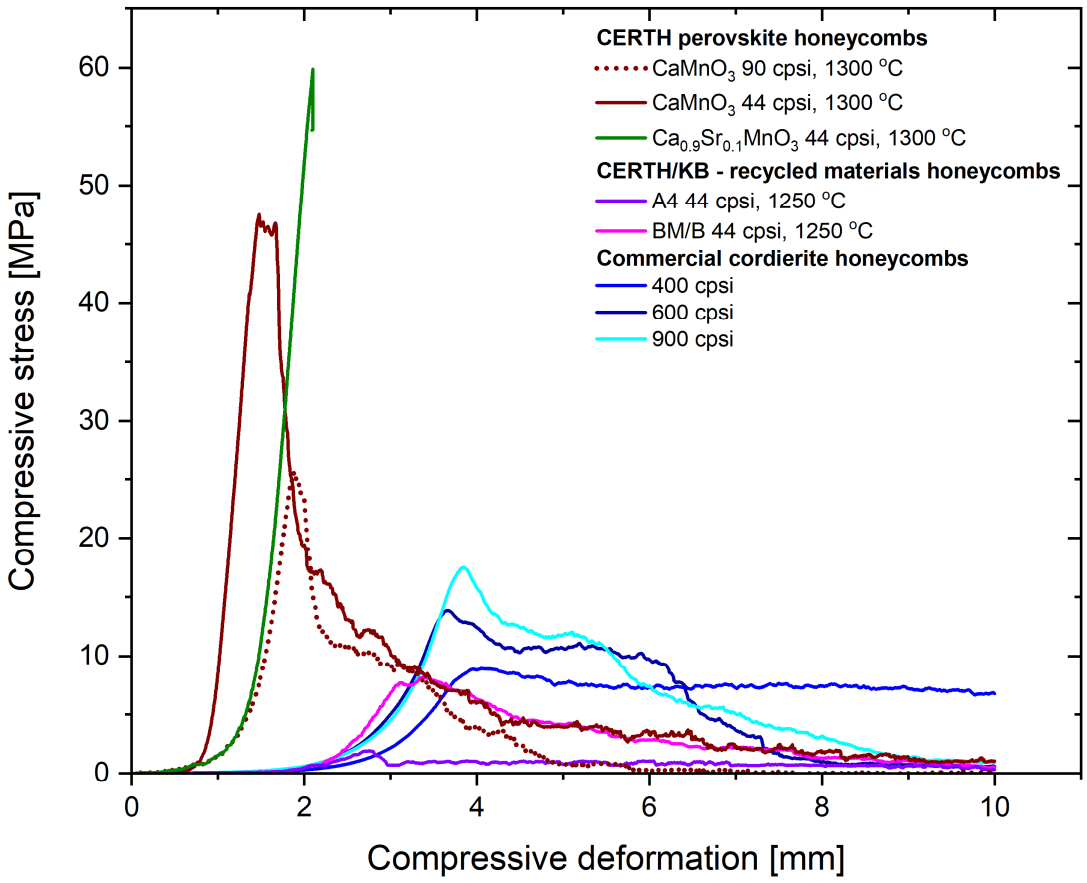

Figure 13*:* Compressive stress-deformation curves of in-house produced CMO-based (CERTH) and reccyled-materials-based (CERTH/KB) honeycombs in comparison to commercial cordierite ones.

Indeed, as can be seen on the figure, their strength is substantially higher than that of commercial cordierite honeycombs and depends, not only on the "structural density"/cpsi number as expected but also on the amount of Sr dopant. Specifically, the CMO 90 cpsi honeycomb (brown dotted line) demonstrated a maximum compressive

stress of 26 MPa. Decreasing the cpsi number in honeycombs of the same composition to 44 – meaning that the specimens have thicker channel walls and higher density (Table 6) - results in almost doubling their maximum compressive strength to 47 MPa (brown solid line). Furthermore, doping the 44 cpsi CMO honeycombs with 10 at % Sr in the A-site resulted in a further increase of envelope density (Table 6) – yet not as prominent as in the case of decreasing the cpsi number - and a further increase of the maximum crushing strength to ca. 60 MPa for the CS10MO honeycomb, followed by abrupt fracture (green line). The beneficial effect of 10 at % Sr mentioned above is further supported from these results. It should be noted that these three honeycomb specimens exhibited very similar wall porosity and mean pore size distribution values (Table 6). Just like in the case of foams, experiments with more specimens per composition and with additional Sr doping are needed and scheduled in order to further establish and quantify such effects.

The non-redox in-house 44 cpsi honeycombs produced out of the two KB materials, exhibited much lower crushing strength values. This is evidently due to a combination of the intrinsic properties of the raw powders used for their shaping and their lower sintering temperature that have resulted in overall lower envelope densities and lower wall porosity. Compressive strength measurements on 44 cpsi honeycombs prepared from T12 (i.e. the 3rd material provided by KB, see D3.1) are currently in schedule.

The crushing strength of commercial cordierite honeycombs ranges between ca. 8-18 MPa and increases with increasing cpsi. It should be stressed here that these structures have a much higher "structural" density (400-900 cpsi) than those of the honeycombs made in-house for the project. This high "density" of the solid grid has a beneficial role, with its "joints" among the channels acting as constraints to deformation and their much higher number in very high cpsi values increases the resistance to compression of the whole body.

Finally, differences with respect to the failure mechanisms of honeycombs and foams can be visualized in Figure 14, where three compressive stress-deformation curves namely these for CMO and CS10MO 60 ppi foams sintered at 1300°C and in Figure 15 for a commercial 900 cpsi cordierite honeycomb are accompanied with representative snaphsots from the camera corresponding to characteristic points along them. Figure 14a and b delineate the effect of 10 % at Sr doping in the case of foams already disussed above, the absence of a clear terminal failure point and the significant deformation of both foams until their copllapse. On the contrary, failure of the cordierite honeycomb seems to start with delamination of outer layers shortly after the maximum crushing strenght is recorded.

It should be again mentioned that all the results correspond to the structures produced or employed with the specific microstructural characteristics (porosity, pore size distribution, solid network density, wall thickness etc.) and do not compare "inherent material properties" like e.g. these of calcium manganites vs. those of cordierite.

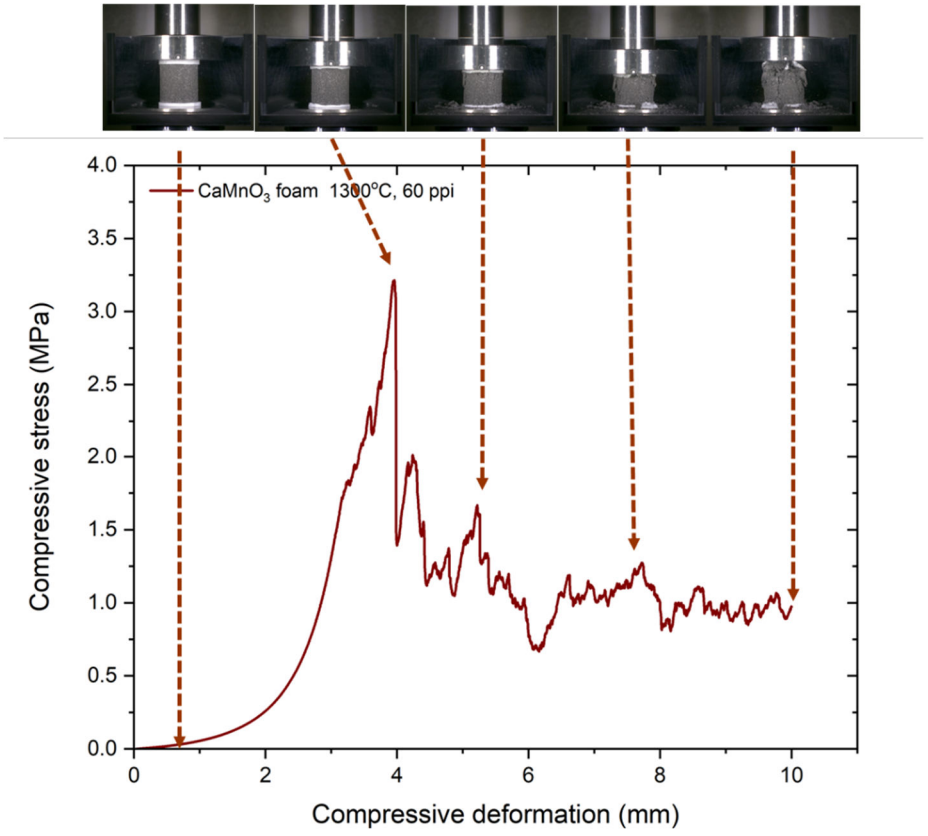

(a)

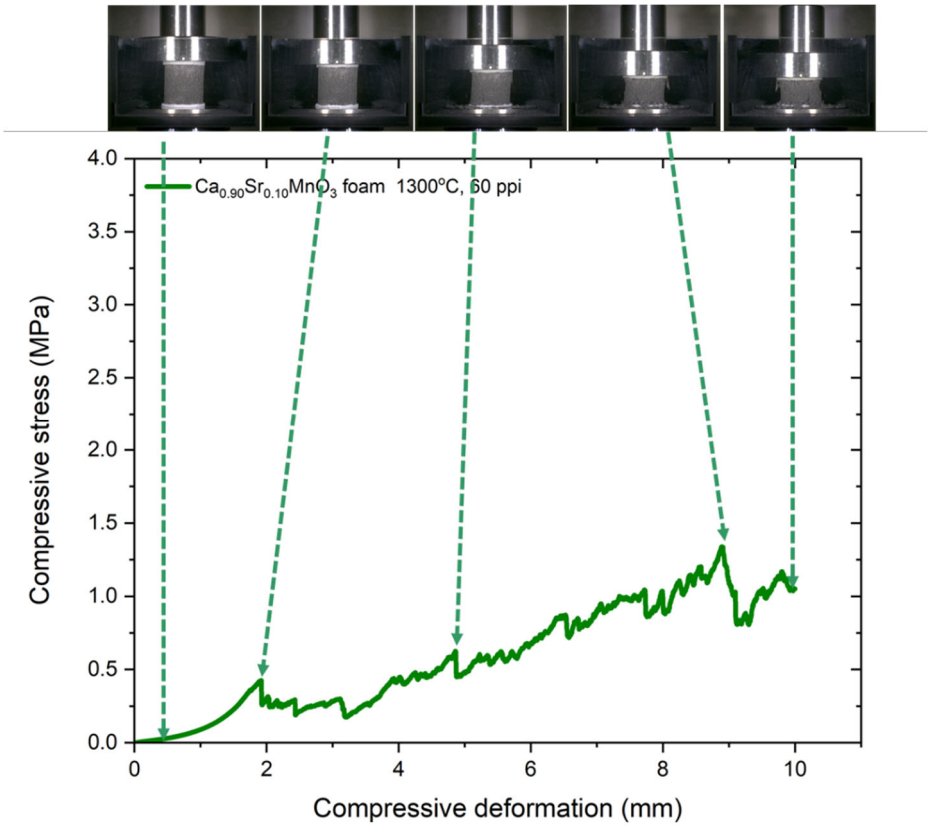

(b)

Figure 14*:* Snapshot photographs from the camera synchronized with the applied load, corresponding to representative points along the compressive stress-deformation curves of 60 ppi foam specimens sintered at 1300ºC: (a) CMO and (b) CS10MO.

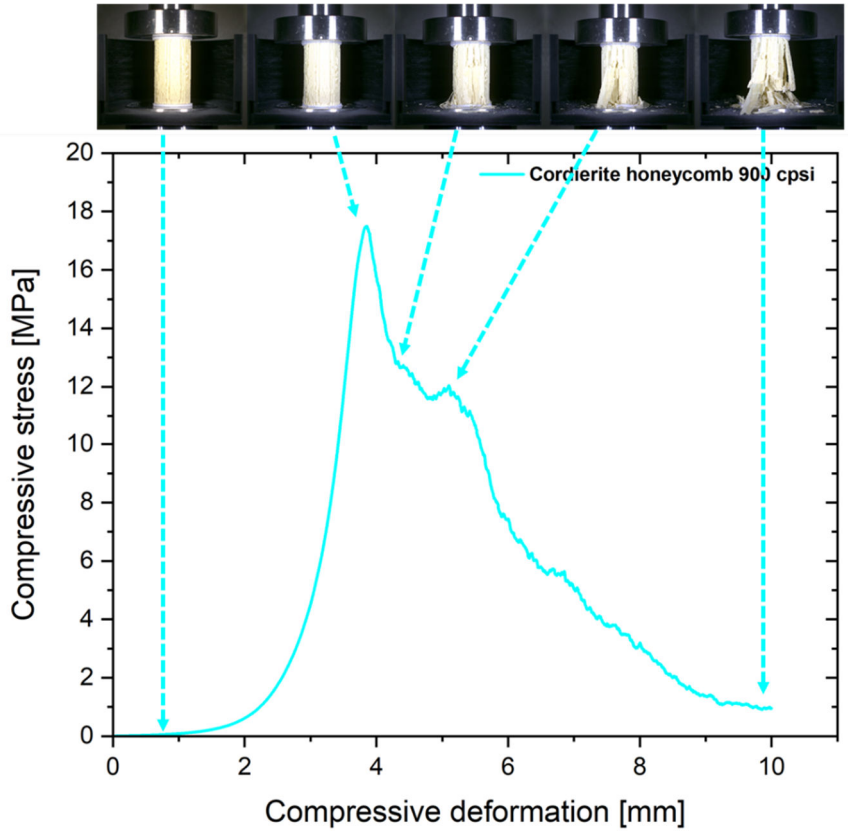

Figure 15*:* Snapshot photographs from the camera synchronized with the applied load, corresponding to representative points along the compressive stress-deformation curves of a commercial 900 cpsi cordierite honeycomb.

3.2 Thermomechanical evaluation via macroscopic, structural and microscopic comparison of pristine and used structures

As mentioned above, two redox structures (i.e. the 60 ppi foam and the 59 cpsi honeycomb), both made of CS10MO, were subjected to > 200 redox cycles. The cycled specimens were carefully removed from the test rig to avoid their damaging as much as possible and inspected both macroscopically and in the Scanning Electron Microscope (SEM). For the honeycomb case, and due to the fact that its experimental evaluation was completed just a few days before the due submission date of the present deliverable, only macroscopic observations are provided herein. It was removed intact from the test rig and will be subjected to crushing strength measurements according to the methodology presented in paragraph 3.1 above, SEM/Energy Dispersive x-ray Spectroscopy (EDS), Hg porosimetry measurements and X-Ray Diffraction (XRD) analysis with the aim to identify differences in its structural, thermomechanical and morphological properties cf. its pristine form. On the other hand, the considerable forces applied for the samples' removal in general resulted to the (limited) damage of the 214-cycled foam since the latter is a

more delicate structure compared to the 59 cpsi honeycomb even in its pristine state. Thus, in the foam case only SEM/EDS and XRD analyses were possible.

The images are collectively provided in Figure 16 and Figure 17 (foam) and Figure 18 (honeycomb) and in all cases direct comparisons between pristine and cycled/used samples are made. It must be noted that the **two CMO honeycombs**, despite the lower number of cycles to which they were subjected (72 and 80; see Table 2), were also examined macroscopically and microscopically. Relevant images are not provided herein for brevity and due to the fact that large part of those has been included, analysed and interpreted in the technical part of the submitted 1st periodic report. To briefly summarise here for the sake of completeness and consistency of the present document, in those cases **a non-detrimental, yet considerable/clearly visible damage was identified**. **The two cycled structures were relatively fragile** (i.e. none of them was removed intact from the reactor holder) and had a **considerable number of visible cracks** that were not evident in its initial pristine state. **A large number of homogeneously distributed micro-cracks were also detected via SEM**. Evidently, this damage was caused by the relatively intense secondary cyclic structural transition between the orthorhombic and cubic form, which was addressed in detailed in submitted deliverables D2.2 and D2.3. As also mentioned and evidenced in D2.2 and for the powder formulations addressed therein, this transition is substantially alleviated for the case of the CS10MO composition.

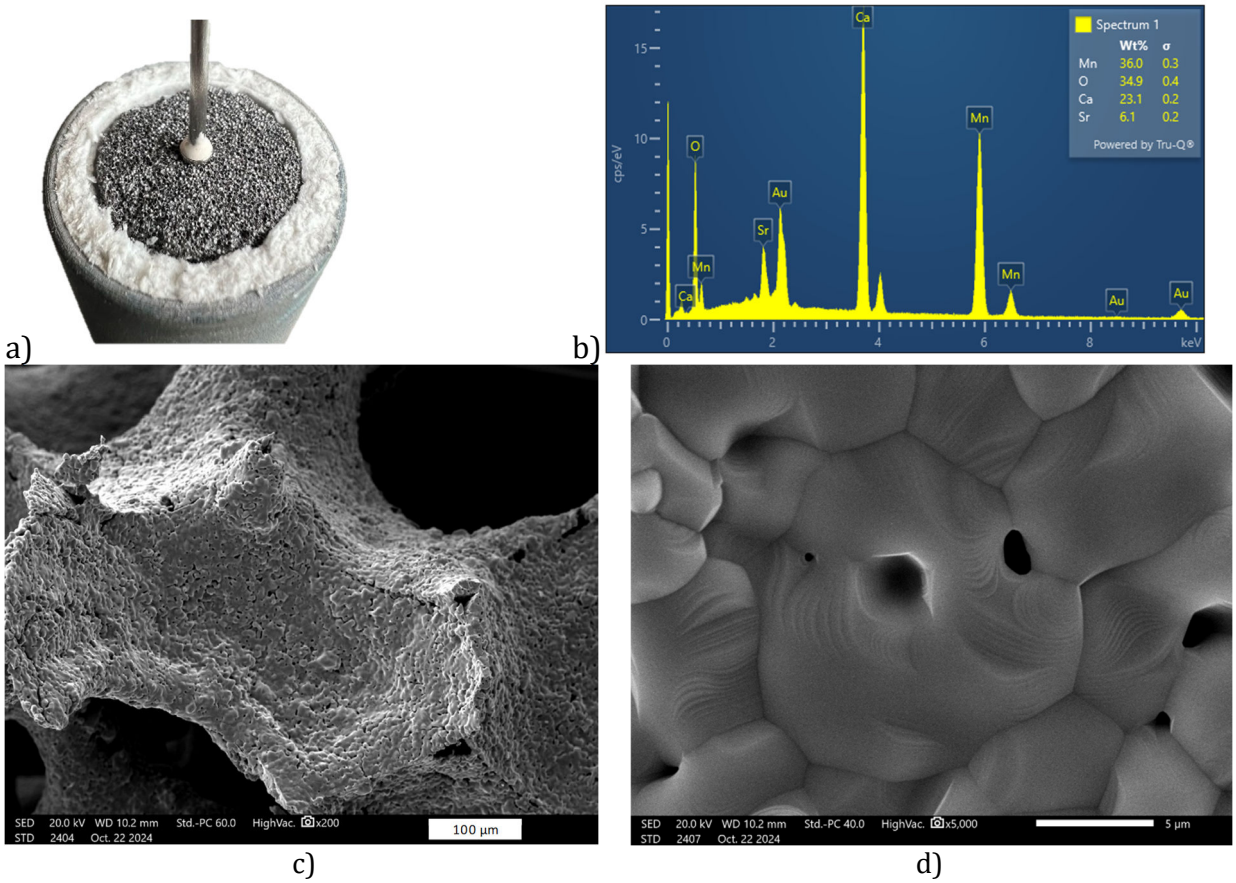

Figure 16: Images referring to a pristine (fresh) CS10MO foam. a) Representative photograph of a 60 cpsi CS10MO foam within its holder (as installed in the test rig of Figure 2); b) results from EDS analysis; SEM images of the structure corresponding to magnifications of c) 200 and d) 5000 times.

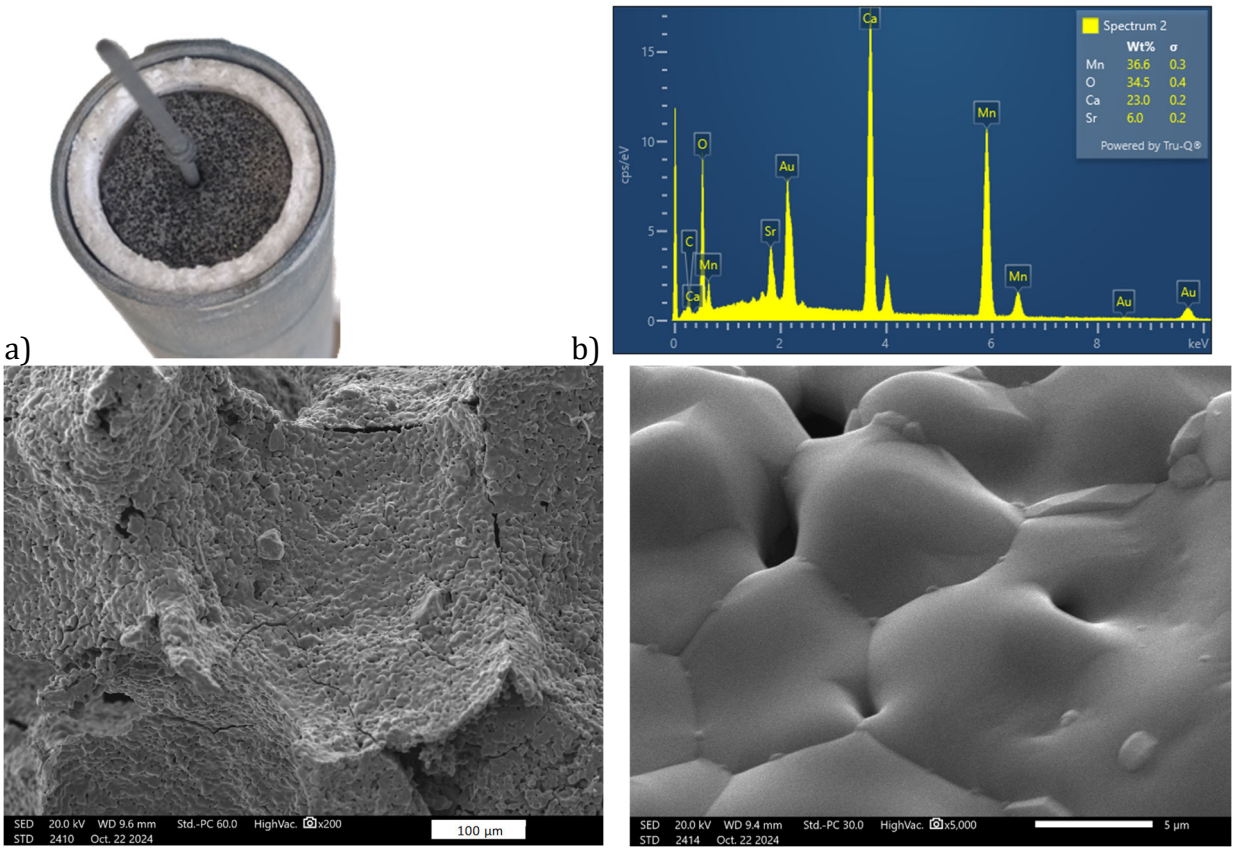

Figure 17: Images referring to a used (fresh) CS10MO foam after 214 thermochemical redox cycles. a) Representative photograph of a 60 cpsi CS10MO foam within its holder (as installed in the test rig of Figure 2); b) results from EDS analysis; SEM images of the structure corresponding to magnifications of c) 200 and d) 5000 times.

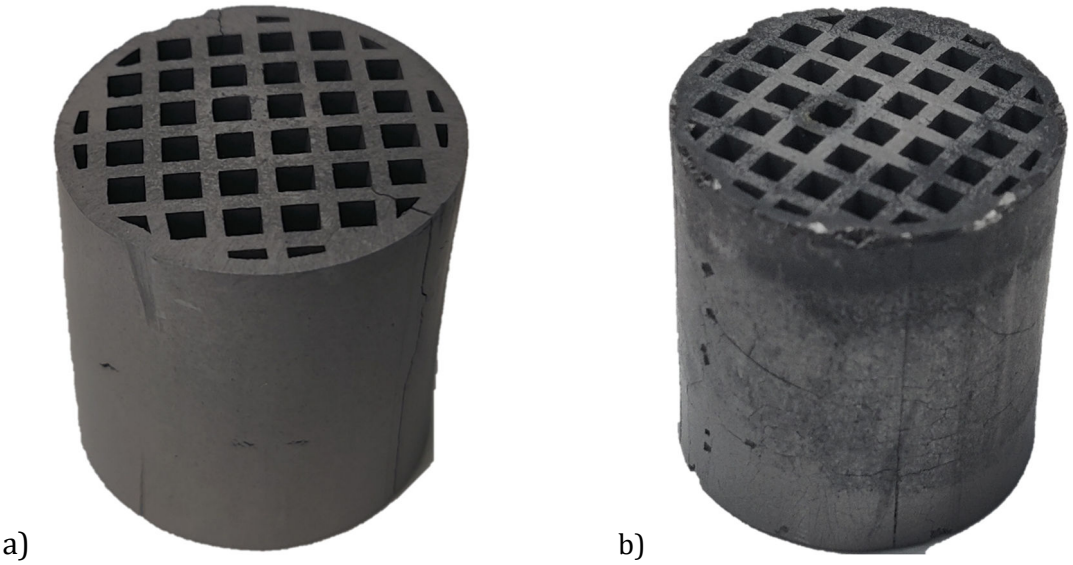

Figure 18: Photographs of the CS10MO honeycomb: a) in its pristine state and b) after completion of 203 redox/thermal cycles and removal from the test-rig

Summarizing the observations based on the images above and additional findings measurements and observations that are not in all cases evident in the images provided, it is concluded that:

- The foam (Figure 17) after 214 cycles had no notable differences macroscopically. Its diameter, as measured in the parts of it that were not damaged by its removal procedure from its holder, did not change measurably while no conclusions could be extracted on its length variation due to cycling because some fragments were broken from one end. In contrast to the CMO honeycombs mentioned above, no cracks or visible deformations were identified. Its overall texture felt/looked a bit brittle compared to its pristine state.
- With respect to micro-structural observations in SEM, no micro-cracks or other deformations were identified. Except for a relatively mild sintering effect, as indicated by the grains' growth in its used state, no other differences were found by comparing the SEM images of the pristine and cycled samples. Based on the EDS measurements, it is evident that the cyclic thermal/ thermomechanical process had no effect whatsoever on the compositional characteristics of the structure. The similarity of the data obtained for the two states was remarkable.
- The 203-cycled CS10MO honeycomb was **robust enough to be removed from the reactor intact**, despite the violent forced applied to it in the process. This provides first solid evidence that the structure retained its mechanical stability to a large extent. Similarly to the foam case, no cracks or deformations were visible on the surface of the structure, apart from the ones already present in its pristine form (already evident in Figure 18a). The honeycomb exhibited a somewhat darker colour cf. its pristine form in a small part of it at the face towards the gas inlet flow side (upper part of the honeycomb in Figure 18b).
- The measured differences in terms of its dimensions before and after the cycles revealed **minor dilation of the overall structure** as its diameter increased by 2.23% and its length by 1.76%. This resulted to a bulk density decrease of about 6.11% cf. its pristine state. **This constitutes a major or even breakthrough improvement compared to past published results referring to redox honeycombs prepared from cobalt oxide-based compositions** that, even for the best case studied and for almost half the number of cycles carried out in ABCSPF project, exhibited relatively major deformations that were clearly immediately identifiable by visual observation [1].
- The scheduled mechanical evaluation (crushing strength measurements) and SEM analyses of this structure are expected to confirm its sufficient resilience when exposed. to the multi-cyclic thermochemically harsh conditions. Complete results will be available before end of February 2025.

Evidently and considering the clear improvement cf. the cycled CMO structures, the addition of Sr is highly beneficial towards stabilization and robustness enhancement of the structured redox material against the very demanding conditions that the high temperature multi-cyclic process imposes to them.

3.3 Phase composition comparison of pristine and used structures

After the long-term tests of the porous structures, comparative X-Ray Diffraction (XRD) analyses were performed on representative samples of pristine specimens (of the same characteristics to the cycled ones) and cycled specimen samples (from both on small fractured pieces ground to powder) to investigate the evolution of phase composition and purity in the course of multi-cycling. The XRD spectra were compared to those of the powder used for the preparation of the shaped structures. **Error! Reference source not found.**Figure 19 and Figure 20 below show two representative cases: the CS10MO 60 ppi foam cycled for 214 cycles and a CMO 59 cpsi honeycomb cycled for 54 cycles, respectively. It can be seen that for both cases, even though there is a slight decrease of the interatomic spacing from the pristine powder to that of the (also pristine) sintered shaped body (shift of the main peak towards higher values of 1/d) this decrease is reversed after multi-cycling with the interatomic spacings of the starting perovskite powders and the cycled specimens to be practically equal. All samples are of high phase purity with respect to the main, targeted $Ca_{0.9}Sr_{0.10}MnO_3$ phase containing small amounts of secondary phases, namely marokite ($CaMn_2O_4$ – both samples) and Ca_2MnO_4 (only the honeycomb). The phase purity of the CMO structure, decreases with increasing number of cycles, in contrast to the trend of the CS10MO one; however, results from more CMO-made cycled structures are needed to further corroborate this trend.

3.4 Porosity and pore size distribution comparison of pristine and used structures

This comparison concerns so far two of the cycled structures included in Table 2 (those of the 1st and 3rd raw) namely a CMO 90/111cpsi honeycomb tested for 72 cycles and a CSM10MO 44/59 cpsi tested for 203 cycles. The comparative analysis of the pristine and the cycled specimens is shown in Figure 21. A first, intuitive conclusion would be that repetitive, cycling sintering of the specimens in the temperature range 650-1100°C, would cause further densification of the porous structures and collapse of smaller pores, i.e. a reduction of porosity and a shift of the mean pore diameter to higher values. This seems to be indeed the case for the CMO honeycomb after 72 cycles. The honeycomb tested for 203 cycles exhibits the same trend with respect to the mean pore diameter, but a reverse trend with respect to porosity. However, taking into account the fact mentioned above, that these values for the pristine state are not measured on the exact same specimen that is eventually cycled but on a specimen of the same specifications and prepared under the same conditions as well as the fact that the observed differences between cycled/used and pristine samples in both cases are not profound, a more realistic conclusion is that the pore structure characteristics of the specimens do not practically change due to multi-cycling, at least within the number of cycles tested so far. Porosimetry measurements of the other two cycled specimens of Table 2 that will help in establishing a more definite trend are currently under way.

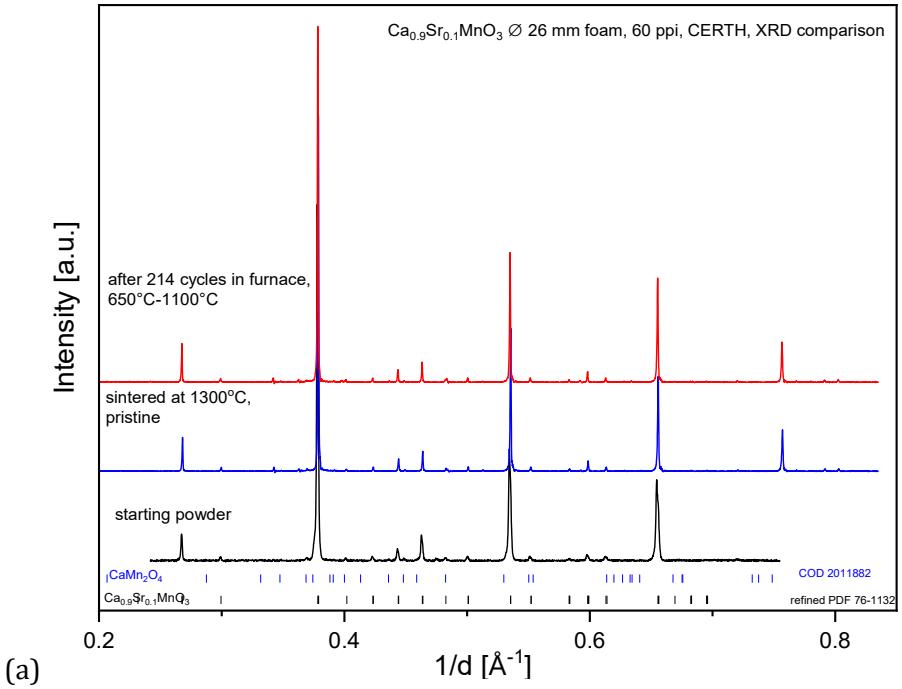

(a)

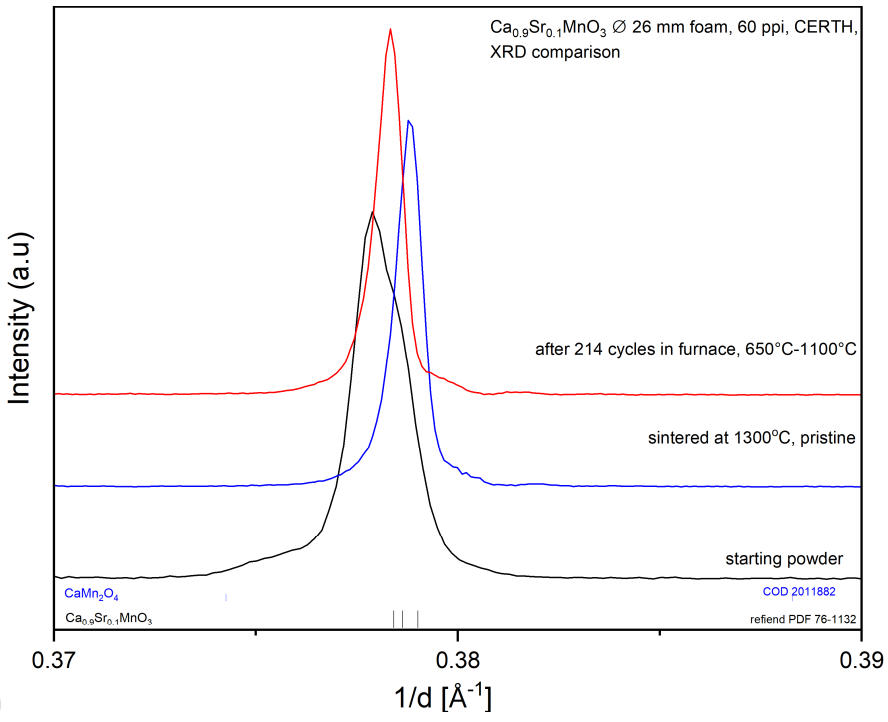

(b)

Pnma	Lattice parameter, Å			Phase fraction, wt.%	
	a	b	c	$CaMnO_3$	$CaMn_2O_4$
Starting powder	5.28875	7.48443	5.28840	95	5
Fresh 60 ppi foam	5.28966	7.47915	5.28802	97	3
214 cycled 60 ppi foam	5.28950	7.48108	5.28761	97	3

Figure 19: Comparative XRD spectra among CS10MO starting powder, pristine foam made out of it and foam cycled for 214 cycles: (a) entire diffraction angle range scanned, (b) magnification around the major peak; table with calculated lattice parameters and phase purity.

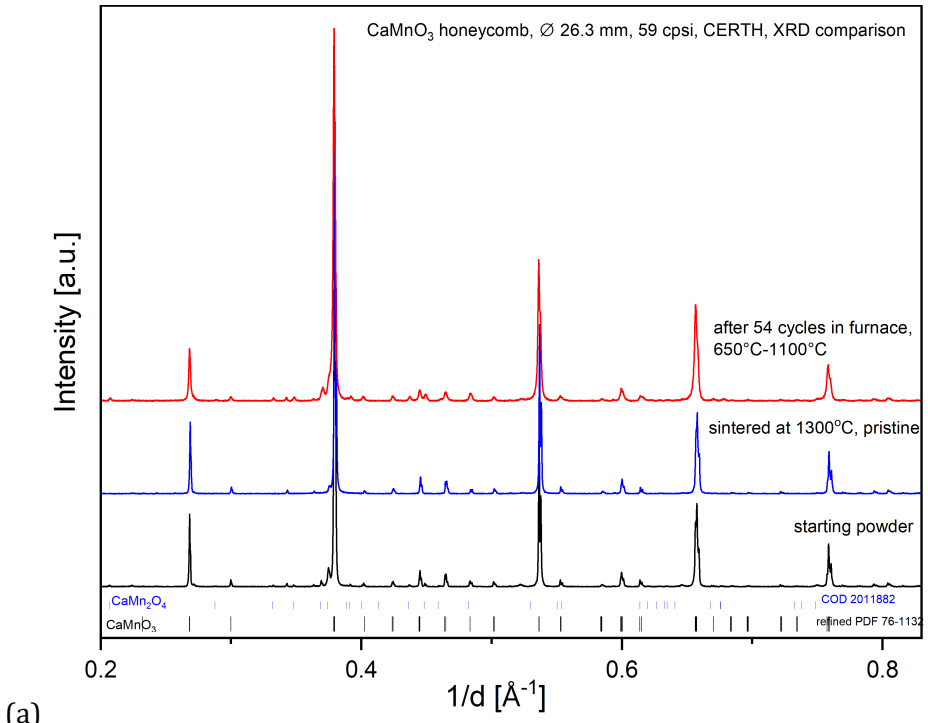

(a)

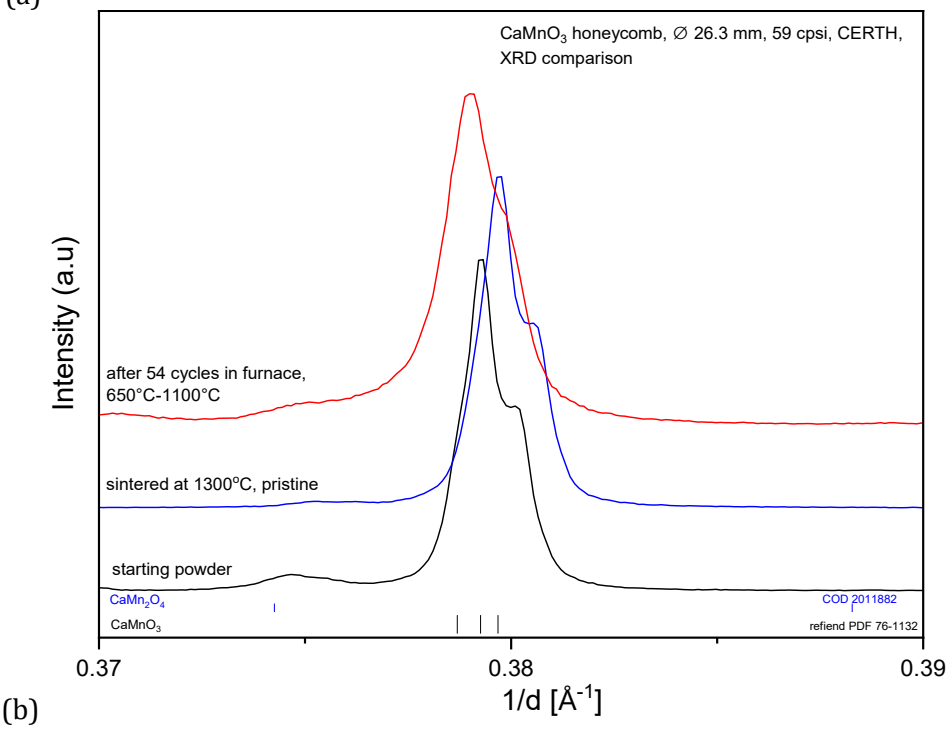

(b)

Pnma	Lattice parameter, Å			Phase fraction, wt.%		
	a	b	c	$CaMnO_3$	$CaMn_2O_4$	Ca_2MnO_4
Starting powder	5.26959	7.45911	5.28324	91.9	3.7	4.4
Fresh 59 cpsi honeycomb	5.26992	7.45878	5.28282	95.2	1.3	3.4
54 cycled 59 cpsi honeycomb	5.27582	7.46281	5.28485	85.1	9.4	5.5

Figure 20: Comparative XRD spectra among CMO starting powder, pristine 59 cpsi honeycomb made out of it and honeycomb cycled for 54 cycles: (a) entire diffraction angle range scanned, (b) magnification around the major peak; table with calculated lattice parameters and phase purity.

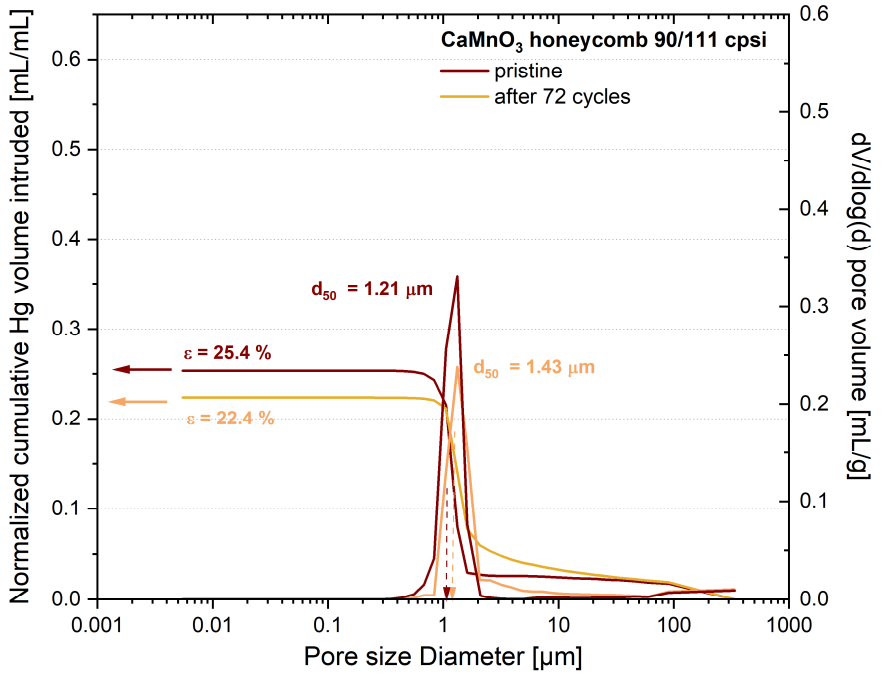

(a)

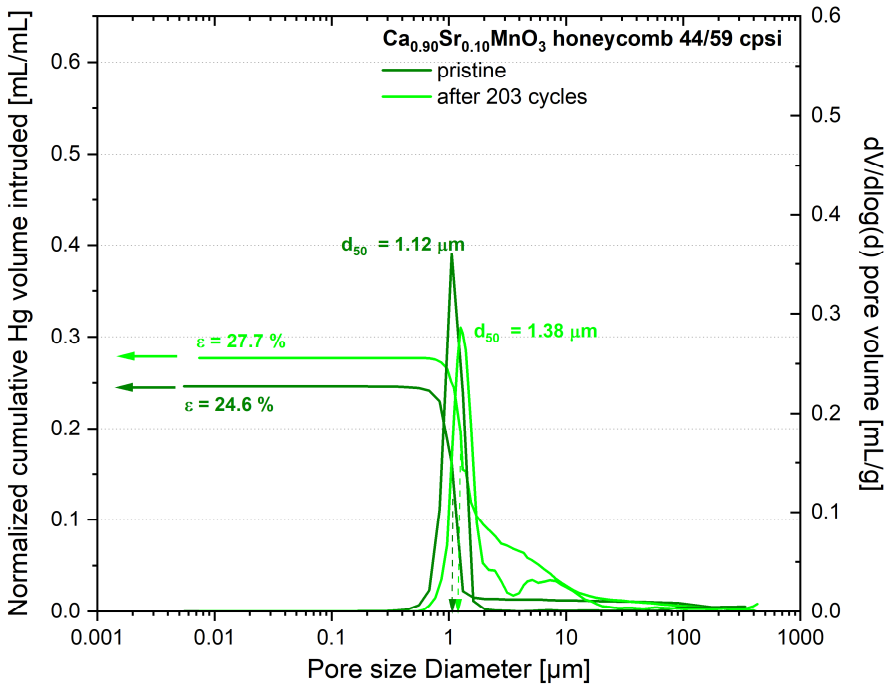

(b)

Figure 21: Comparative Hg porosimetry analysis between pristine, as-sintered honeycomb specimens and after redox thermal cycling: (a) CMO honeycomb 90/110 cpsi tested for 72 cycles, (b) CS10MO honeycomb tested for 203 cycles.

4. Conclusions

The relevant experimental campaigns provided solid proof that the CMO and CS10MO based redox structures evaluated in WP3 are able to demonstrate substantial thermochemical heat effects under properly designed operating protocols. These heat

effects result to a substantial thermal boosting effect, which is one of the main targets of the project. **The temperature of air passing through the structures in the course of the exothermal oxidation can be increased by up to 140°C while the respective temperature increase on the surface of the structures was found to be up to 206°C.** The redox operation of the perovskite structures is repeatable and stable and the addition of 10% at Sr (CS10MO case) is highly beneficial on the energetic and redox performance of the structured bodies. A clear positive effect on the structural stability is also evident cf. the undoped CMO structures. The use of relatively dense structures (i.e. high bulk/geometrical density) is beneficial in terms of energetic performance and thus future scaled-up structures to be manufactured in the frame of project's activities should consider this general guideline. The crushing strength of the extruded perovskite honeycombs are comparable or higher than state of the art commercial cordierites and this provides confidence for the structural viability in the course of the targeted hybrid thermal/thermochemical operation. The multi-cyclic redox operation (i.e. > 200 cycles for two different structures of CS10MO) has essentially no effect on the composition of the structure, which is in full agreement with the experimentally validated stable cycle-to-cycle redox performance. Apparent correlations of important operating parameters of the process (temperature, pressure, reduction extent) to the energy density/effective reaction enthalpy and the non-stoichiometry parameter (δ) were extracted and are currently used for the necessary numerical studies of WP4.

The results presented here provide solid **proof for the successful completion of project's milestone *M2: Structured objects made of optimized material compositions with maximum active material content selected for manufacture of the proof-of-concept unit*** to a large extent by M27. To complete at 100% the requirement of structural stability of redox bodies subjected to > 200 cycles and quantify potential differences, comparative crushing strength measurements of the 203 times cycled CS10MO 59 cpsi honeycombs cf. pristine samples (already measured) are scheduled for the next period.

Next steps will include additional extrusion campaigns and redox thermochemical evaluation of small-scale redox structures with the CS10MF5O and CS10MF10O compositions (see also deliverable D3.1) while the information presented here and the main guidelines produced will be also considered for the scaled-up extrusion studies of WP5.

5. References

[1] G. Karagiannakis, C. Pagkoura, E. Halevas, P. Baltzopoulou, A. G. Konstandopoulos, Cobalt/cobaltous oxide-based honeycombs for thermochemical heat storage in future concentrated solar power installations: Multi-cyclic assessment and semi-quantitative heat effects estimations, Solar Energy, 133, 394-407 (2016)